DOI: 10.1002/adfm.201802592

Article type: Review

Gas Humidification Impact on the Properties and Performance of Perovskite-Type Functional Materials in Proton-Conducting Solid Oxide Cells

Wei Wang, Dmitry Medvedev, Zongping Shao**

Dr. W. Wang, Prof. Z. Shao

WA School of Mines: Minerals, Energy and Chemical Engineering (WASM-MECE), Curtin University, Perth, WA 6845, Australia

E-mail: zongping.shao@curtin.edu.au

Dr. D. Medvedev

Laboratory of Electrochemical Devices Based on Solid Oxide Proton Electrolytes, Institute of High Temperature Electrochemistry, Yekaterinburg 620990, Russia

E-mail: dmitrymedv@mail.ru

Dr. D. Medvedev

Ural Federal University, Yekaterinburg 620002, Russia

Prof. Z. Shao

Jiangsu National Synergetic Innovation Center for Advanced Material, State Key Laboratory of Materials-Oriented Chemical Engineering, College of Chemical Engineering, Nanjing Tech University, Nanjing 210009, China

Keywords: chemical expansion, proton-conducting materials, solid oxide electrochemical cells, transport properties, water vapor partial pressure

Fuel cells and electrolysis cells as important types of energy conversion devices can be divided into groups based on the electrolyte material. However, solid oxide cells (SOCs) based on conventional oxygen-ion conductors are limited by several issues, such as high operating temperature, the difficulty of hydrogen purification from water, and inferior stability. To avoid these problems, proton-conducting oxides are proposed as electrolytes for SOCs in electrolysis and fuel cell modes. Since water vapor partial pressure (pH_2O) is one of the main parameters determining the proton concentration in proton-conducting oxides (characteristics of which can be either improved or deteriorated), the pH_2O control is extremely important for the optimization of the devices' performance and stability. This review provides an overview of the research progresses made for proton-conducting SOCs, especially for the impact of gas humidification on the operability and performance. Fundamental understanding of the main processes in proton-conducting SOCs and design principles for the key components are summarized and discussed. The trends, challenges and future directions that exist in this dynamic field are also pointed out. This review will inspire interest from various disciplines and provide some useful guidelines for future development of proton-conductor-based energy storage and conversion systems.

1. Introduction

Complex oxides with meaningful proton transfer capability at certain conditions are proposed to be promising functional materials for solid oxide cells (SOCs), which form the basis of highly efficient, environmentally friendly and economically attracted electrochemical devices and technologies.[1–4] If the ionic transporting capability dominates over the electronic one, such conducting materials can be used as electrolytes for solid oxide fuel cells (SOFCs), solid oxide

electrolysis cells (SOEC), hydrogen sensors and hydrogen pumps,[5–8] operating on the principles of chemical energy conversion to electricity, electricity to chemicals, hydrogen detection and hydrogen separation, respectively. If electronic transport is comparable with (or higher than) the ionic one, electrode-free membranes for hydrogen-separation reactors and electrode materials for electrode-based SOCs can be purposefully designed.[9] Unconventional proton transport for oxide materials allows the unique processes to be also carried out, for example, a precise H/D/T-isotope analysis, conversion of harmful (NO_x) or widely available compounds (CO_2) to harmless and valuable products (N_2, CO), conversion of saturated hydrocarbon (CH_4, C_2H_6) to unsaturated or aromatic compounds (C_2H_4, C_6H_6), hydrogen compression and etc.[10-13]

A proton-conducting electrolyte is a heart for the proton-conducting SOCs. Such materials demonstrate superior proton conductivity in the temperature range of 300-700 °C, owing to high both concentration and mobility of proton charge carriers in comparison with similar parameters of the oxygen-ionic electrolytes (stabilized ZrO_2, doped CeO_2 and doped $LaGaO_3$).[14,15] This unique feature of proton conductors has attracted increasing interests for the development of the low- and intermediate-temperature solid oxide electrochemical cells.

When solid oxides are in contact with hydrogen-containing gas components (H_2, NH_3, H_2O) at elevated temperatures, a proton transport is formed. In the case of redox-stable systems (e.g., electrolytes), the highly mobile proton defects ($OH_O^{\bullet}$) appear through the interaction of existing oxygen vacancies ($V_O^{\bullet\bullet}$) with steam, as illustrated by equation (1) presented in Kroger-Vink formalism.[16] Energetically, this process takes an intermediate place between physical adsorption of water and deep chemical interaction with the formation of hydroxide phase(s). Therefore, the

proton-conducting materials should have good structural stability (no decomposition) when they are hydrated.

$$V_O^{\bullet\bullet} + O_O^x + H_2O \rightleftarrows \quad (1)$$

By applying the law of mass action to the equation (1), the dependence of proton defects concentration on the water vapor partial pressure can be presented as:

$$[OH_O^{\bullet}] = K_w^{1/2}[V_O^{\bullet\bullet}]^{1/2}[O_O^x]^{1/2}\left(pH_2O\right)^{1/2} \quad (2)$$

Here K_w is the equilibrium constant of the reaction shown in equation (1). According to equation (2), the water vapor partial pressure is a key parameter affecting the ion transport (particularly, proton on account of $OH_O^{\bullet}$, oxygen-ion on account of $V_O^{\bullet\bullet}$) and electron transfer. Correspondingly, the water concentrations in oxidizing and reducing atmospheres determine the functionality and performance of electrochemical devices based on these electrolytes.

Although there were several excellent reviews published on the topic of proton-conducting oxides in the past years,[6,7,9,10,13,14] these reviews were mainly aimed at the development and design of materials for the applications in SOCs. In this review, we focus on the effect of gas moisturizing (humidification) on the functionality, properties and performance of the proton-conducting materials to provide some useful guidelines on the optimization of electrochemical proton-conducting systems (symmetrical cells, fuel cells and electrolysis cells) by varying and controlling the water vapor partial pressures. Due to excellent mobility of protons and their low activation barrier, the proton-conducting electrolytes and corresponding electrochemical devices show promising performance below 500 °C. However, the proton-conducting electrolytes are almost fully hydrated

under such low temperatures. This does not allow us to reveal the pH_2O influence on the functionality of the proton-conducting perovskite oxides. Thus, we discussed the progress of the proton-conducting materials above 600 °C, when a hydration limit hasn't been reached in these electrolytes, which can respond to the pH_2O changes significantly.

2. Proton-conducting electrolytes as a basis for SOCs

A SOC is composed of two electrodes and one electrolyte, where the electrolyte is sandwiched by the two electrodes. This electrolyte membrane allows the transfer of ions (O^{2-} or H^+) from one "electrode|electrolyte" interface to another one, whereas the electrochemical oxidation/reduction reactions occur over the electrodes. In the case of the electrolytes with proton conductivity, the principles of different types of SOCs are summarized in **Figure 1**. Gas tightness is one of the most important requirements for proton-conducting SOCs. In other words, the proton-conducting membrane separates two different gases without any mixing. Along with highly dense structure, the electrolytes should have excellent ionic and negligible electronic conductivity to suppress the undesirable self-starting electrochemical reactions. Since the proton-conducting processes occur with the participation of many gas components, the electrolytes are needed to possess a superior structural stability and a good tolerance against the interactions with gases as well as other functional components in SOCs (cathode, anode, interconnector and sealant). The constituent materials should be thoroughly selected by considering their thermal properties during different technological stages (co-sintering, electrode sintering, start-up, cool-down and thermo-cycles) to avoid any cracking, delamination and leakage.

It can be seen that the proton-conducting membrane in SOC is simultaneously in contact with both cathodic and anodic atmospheres with different partial pressures of oxygen (pO_2), hydrogen (pH_2) and water vapor (pH_2O), etc. Some of these partial pressures are the potential-determined parameters of transport behavior of the proton-conducting electrolytes. The description of their transport properties is convenient to carry out using the quasi-chemical model. The defect formation and interaction processes for $A^{2+}B^{4+}_{1-x}M^{3+}_{x}O_{3-\delta}$ can be presented as follows:[17,18]

$$M_2O_3 \xrightarrow{"BO_2"} M'_B + V_O^{\bullet\bullet} + 3O_O^x \quad (3)$$

$$V_O^{\bullet\bullet} + O_O^x + H_2O \overset{K}{\rightleftarrows} \quad (1)$$

$$1/2O_2 + V_O^{\bullet\bullet} \overset{K}{\rightleftarrows} h^{\bullet} \quad (4)$$

$$O_O^x \overset{K}{\rightleftarrows} 1/2O_2 + 2e' \quad (5)$$

Here, M'_B is an acceptor dopant occupying the B-site, O_O^x is the oxygen-ion in its regular site, $h^{\bullet}$ and e' are the holes and electrons, K_p and K_n are the equilibrium constants of the reactions (4) and (5). Considering a general electroneutral condition (or its particular cases)

$$[M'_B] + [e'] = 2[V_O^{\bullet\bullet}] + [OH_O^{\bullet}] + [h^{\bullet}] \quad (6)$$

as well as a balance of ions

$$[O_O^x] + [V_O^{\bullet\bullet}] + [OH_O^{\bullet}] = 3 \quad (7)$$

the dependences of defects concentration on the pO_2 and pH_2O variation are shown in **Figure 2**. This Figure describes the bulk structure of proton-conducting martials, which are free from the defects interaction resulting in change in the concentrations of mobile charge carriers.[19] Moreover, the impacts of surface and grain boundaries are not considered in the presented model (equation (1)–(7)), which are always chemically different in comparison with the bulk region of the materials.[20]

According to Figure 2, a drop of pO_2 resulted in the corresponding decrease in the hole defect concentration. At the same time, the increase in pH_2O led to a decrease in the levels of both oxygen-ionic and p-type electronic conductivities. This tendency is also suitable for the low- and intermediate-temperature SOCs since the rapid improvement of proton transport with an increase in pH_2O can also be achieved at reduced temperatures.

The purposeful changes of pO_2, pH_2O and temperatures enable the enhancement of the transport properties of proton-conducting membranes. However, the relationship between other functional materials of SOCs and external changes (particularly, pH_2O) may be different and the thorough analysis of reported data is required to reveal the main regularities.

3. Functional materials of proton-conducting SOCs

3.1. Electrolytes

Among different representatives of proton-conducting oxides in SOCs, the $BaCeO_3$- and $BaZrO_3$-based materials are most widely studied perovskite oxides.[21] In this section, we primarily focus on these two systems with a great emphasis while some other important proton-conducting oxides are also summarized.

3.1.1. Features of hydration

Protons are not an inborn part of oxide materials, since the proton-conducting-related properties only appeared after the hydration process (equation (1)). Dissociative absorption of steam occurs with the participation of oxygen vacancies. They were created by the acceptor doping way (equation (2)), which determined the maximal level of proton concentrations (hydration limit). Since the reaction in equation (1) is exothermic, the proton concentration decreased with the increasing temperature shown in Figure 2e-h and the following equation:

$$K_w = \exp\left(\frac{\Delta S^o}{R}\right)\exp\left(-\frac{\Delta H^o}{RT}\right) = \frac{[OH_O^{\bullet}]^2}{[V_O^{\bullet\bullet}][O_O^x]pH_2O} \quad (8)$$

where ΔH^o and ΔS^o are the standard molar enthalpy and entropy, respectively. Some proton-conducting oxides with these parameters after hydration are listed in **Table 1**.[24-34]

The temperature is one of the most influential factors to affect the defect interaction (especially at relatively low temperatures and high defect concentration[19]), surface and grain boundary chemistry[22]. In addition, the temperature also has a strong effect on the experimental level of $[OH_O^{\bullet}]$ at a specific condition. As a result, a reduced amount of mobile oxygen vacancies was achieved due to the structural features of some perovskites.[23,32]

From the chemical aspect, Kreuer presented the direct correlation between the thermodynamic parameters of the hydration and the basicity of ABO_3 perovskites.[28] More precisely, the equilibrium constant (equation (8)) was found to be increased in the sequences of Ca → Sr → Ba (A site) and Ti → Nb → Sn → Zr → Ce (B site). As a result, $BaCeO_3$- and $BaZrO_3$-based perovskite oxides demonstrated the highest hydration capability, the highest concentrations of proton charge

carriers in their perovskite structures and the highest protonic conductivity. However, these $BaCeO_3$- and $BaZrO_3$-based systems exhibited a lower water uptake capability in comparison with the theoretically predicted level, corresponding to a full hydration of oxygen vacancies, $[OH_O^{\bullet}] = [M_B^{/}]$, as shown in **Figure 3**. There are several reasons leading to these experimental results.[19-22] The BaO evaporation and redistribution of the acceptor dopants between A site and B site of ABO_3 structure is reported as one of the reasons;[21] this results in an effective decrease in the amount of oxygen vacancies, which is regulated by the acceptor dopant concentration as depicted in equation (3). An inhomogeneity of surface regions and grain boundaries can be considered as another reason of the low (overall) proton concentration and hydration capability.[20,22] Finally, the existence of simple ($\{OH_O^{\bullet} - M_B^{/}\}^x$, $\{V_O^{\bullet\bullet} - M_B^{/}\}^{\bullet}$) and complex ($\{M_B^{/} - OH_O^{\bullet} - M_B^{/}\}^{/}$, $\{M_B^{/} - V_O^{\bullet\bullet} - M_B^{/}\}^x$) defects' associates is found to be the decisive factor for the observed differences in theoretical and experimental water uptake capability, especially at relatively low temperatures, when these associates are stable.[19] The evident ways of improving the experimental levels of water uptake capability and proton concentrations should be thorough control of the Ba-stoichiometry, the decrease of the impurities coming from the initial powders or some technological steps (such as milling, grinding, and treatment), and the achievement of conditions favorable for the dissociation of the defects and defect-based associates.

3.1.2. Crystal structure

Although $BaCeO_3$ and $BaZrO_3$ belong to perovskite oxides with a formula of ABO_3, their crystal structures are different, which can cause some differences in the proton transport. The nominally pure $BaCeO_3$ and $BaZrO_3$ exhibited orthorhombic and cubic structures at room

temperature, respectively.[21] This difference can be assigned to the ionic radii difference of the B-site elements (Ce^{4+} and Zr^{4+}) occupied B-site and can also be described by the Goldschmidt tolerance factor:[35]

$$t = \frac{r_{Ba^{2+}}^{XII} + r_{O^{2-}}^{VI}}{\sqrt{2}\left(r_{B^{4+}}^{VI} + r_{O^{2-}}^{VI}\right)} \quad (9)$$

Where r is the ionic radius of the ions in corresponding coordination states. This factor is associated with the degree of stability or distortion of the perovskite structure. If the tolerance factor is close to 1.0, the formation of a cubic structure is energetically favorable. With an increase of tolerance factor up to 1.04 or a decrease down to 0.71, some distortions of the perovskite structure can be formed, such as tetragonal, rhombohedral, orthorhombic or monoclinic ones. Using Shannon system, the tolerance factors were around 0.94 and 1.00 for $BaCeO_3$ and $BaZrO_3$, respectively, agreeing well with their crystal structures.[36]

The structural changes were especially clear by using a system based on $BaCeO_3$ and $BaZrO_3$ solid solutions (**Table 2**),[38-44] for which a sequence of phase transitions was observed. It should be noted that different structures existed for the material with the same composition. Since the tolerance factor actually kept constant, some other factors also affected the phase structures in the $BaCeO_3$–$BaZrO_3$ system. Temperature and pH_2O also have some contributions to such factors (**Figure 4**) although their effects on the crystal structure are opposite.[45,46] The symmetry of perovskite structure increased with increasing the temperature due to octahedral tilting diminishing and decreased with increasing the water vapor content, suggesting that the significant distortion of the

lattice was relevant to the material's hydration capability. This will also lead to a chemical expansion effect, which will be described in detail in the next section.

3.1.3. Chemical expansion

The hydration effect of the proton-conducting materials resulted in a considerable structural change (Figure 4c), which not only led to the phase transition(s) but also to the lattice expansion. Recently, the thermo- and chemo-mechanical properties based on the hydration capability has been intensively studied for the doped $BaCeO_3$, $BaZrO_3$ and $BaCe_{1-x}Zr_xO_3$ systems. Different experimental and theoretical studies were performed by Uda et al.[46-48], Andersson et al.[49,50], Tsidilkovski et al.[51], Jedvik et al.[52], Bjørheim et al.[53] and Mather et al.[54]. The obtained results demonstrated that the proton formation led to a lattice expansion compared with the initial one containing oxygen vacancies (**Figure 5**a and b).[50,52,55] Based on the numerical estimation, the effective ionic radii of $V_O^{\bullet\bullet}$, $OH_O^{\bullet}$ and O_O^x were 1.18, 1.35 and 1.40 Å, respectively.[49] It indicated that the creation of oxygen vacancies by acceptor doping always resulted in the lattice contraction by assuming conditionally that the effective ionic radii of cations were not changed with such a doping. On the other hand, the lattice expansion was accompanied by the filling of oxygen vacancies with water vapor and the formation of stable proton defects.

The chemical expansion of the proton-conducting materials under gas humidification increased with the increasing in the basicity of oxides and the amount of the acceptor dopant (Figure 5c), which was responsible for a sufficient amount of oxygen vacancies. According to the comparative analysis presented in the literature,[52,56] chemical expansion coefficient varied in a wide

range of 0.01–0.2 depending on the chemical composition of the $BaCe_{1-x-y}Zr_xM_yO_{3-\delta}$ system, including Zr content (x), type of dopant (M) and its concentration (y).

It is interesting that relative expansion of the proton-conducting materials can reach a quite high value under conditionally isothermal dwell. Based on the results of Andersson et al., the relative changes in the calculated unit cell volumes of $BaCe_{0.8}Y_{0.2}O_{3-\delta}$ in dry and wet oxygen atmospheres at 500-800 °C is equivalent to change in the cell volume with a 200 °C increase in the temperature at a constant gas composition (dry oxygen, Figure 5d).[50] Such a high degree of the lattice expansion might be a reason of their mechanical stress, which was one of the essential problems in SOCs. In addition, the relative change of unit cell parameters (or other dimension characteristics) did not depend substantially on the pO_2 variation due to the high stability of the anionic sublattice. This can be realized even for the $BaCeO_3$-based materials, which contained the Ce element with variable oxidation states (Ce^{4+}/Ce^{3+}). On the other hand, many oxygen electrodes suffered from the relative dimension shrinkage/expansion induced by the pO_2 change.[57] Therefore, the creation of good adhesive electrolyte/electrode contacts with no destruction under both pO_2 and pH_2O variation is then critical for the stable operation of SOCs.

3.1.4. Stability

High basicity of the oxides is favorable for the formation of stable proton defects in the crystal structure due to the more exothermic hydration enthalpies. From this viewpoint, $BaCeO_3$-based materials are demonstrated to be good ionic conductors with the highest values of total proton conductivity. However, the stability of proton defects was not satisfied at both low- and high-

temperature regions. From the one side, the concentration of proton charge carriers decreased with the increasing temperature. At the temperatures higher than 700-900 °C (depending on the materials composition and ambient gas conditions) the effect of concentration overwhelmed the effect of the increasing protons mobility, resulting in a decrease in the proton conductivity.[28,58] The proton concentration at high temperatures can be partially increased by providing a higher pH_2O level, which shifted the equilibrium of reaction (1) to the right. From the other side, the character of proton/oxygen bond in $OH_O^{\bullet}$ was changed to the ionic bonds with the formation of hydroxyl groups (OH^-), which led to the decomposition of the proton conductors, especially at low temperatures and high steam concentrations:[59,60]

$$BaCeO_3 + H_2O = Ba(OH)_2 + CeO_2 \qquad (10)$$

For example, pure $BaCeO_3$ was thermodynamically stable in the high-temperature region and started to react with steam at the temperatures below 400 °C.[60]

Carbonate phases were then formed in humid atmospheres with the existence of trace amount of CO_2:

$$Ba(OH)_2 + 2CO_2 = Ba(HCO_3)_2 \qquad (11)$$

$$Ba(OH)_2 + CO_2 = BaCO_3 + H_2O \qquad (12)$$

Thermodynamic calculations suggests that H_2O is a less aggressive component for $BaCeO_3$-based materials than CO_2 since $BaCeO_3$-based materials are stable at the temperatures higher than ~1040 °C, while they are decomposed in the CO_2-containing atmospheres at lower temperatures.[60]

Many efforts have been devoted to the maintenance of high proton conductivity and enhancement of chemical stability of the $BaCeO_3$-based materials.[21,61] One possible way is the partial substitution of basic ions with some dopants, which decreased the basicity with an increased tolerance factor. Most frequently, the modification of $BaCeO_3$ was carried out by partially substituting Ce^{4+} cations in the B-site (**Figure 6**a). The chemical stability of the modified oxides was significantly enhanced in both H_2O- and CO_2-containing gases (Figure 6b), allowing the materials to be used stably in the intermediate-temperature range.[64-75] The proton transport was also maintained in this way since the oxides formed by complete Ce^{4+} substitution by the different acceptor, isovalent and donor dopants (for example, $Ba_2In_2O_5$, $BaZrO_3$, $BaSnO_3$) also have proton transport capability.[37,62,63] However, their proton conductivities were lower than those of $BaCeO_3$-based materials, which can be assigned to several reasons. Firstly, the free volume and migration channels size of the unit cell decreased although the crystal structures symmetry and tolerance factor value increased at the same time. Correspondingly, the mobility of charge carriers decreased. Secondly, some introduced dopants possessed refractory nature in comparison with cerium ions. In this situation, the grain boundary conductivity considerably dropped due to the smaller grain size and higher grain boundary density (Figure 6c).[76-78] Thirdly, the oxygen vacancy concentration decreased when the donor-type cations were used as the dopants.

The ceramics of the $BaCe_{1-x-y}Zr_xM_yO_{3-\delta}$ system are considered as the most promising materials for SOCs since some functional characteristics can be achieved by tailoring the Ce/Zr ratio rationally. Starting from primary results reported by Wienströer and Wiemhöfer in 1997,[79] Ryu and Haile in 1999,[80] more than 300 works on this system have been published up to now.

3.1.5. Ceramic and mechanical properties

The ideal proton-conducting ceramic electrolytes should have well-developed grains, no porosity and "pure" grain boundaries, which can be determined by prehistory of the prepared powders (mean particle size, particle size distribution), technological modes (temperature and dwelling time) and their own chemical composition. For example, the sintering temperature should be increased considerably to obtain highly-dense ceramics with increased zirconium concentration (x) in the above-mentioned $BaCe_{1-x-y}Zr_xM_yO_{3-\delta}$ system if other conditions kept unchanged.[37] The possibilities of different synthesis methods allowed the production of active and pure-phase powders and, consequently, desirable ceramics were developed and reported,[81,82] particularly for $BaCeO_3$ and $BaZrO_3$-based materials.[83,84] This section aims to focus on the mechanical properties of ceramic materials.

Depending on the architecture of the electrochemical devices, the proton-conducting electrolytes can act as a support as well as a thin film. To decrease the ohmic resistance (R_o), many SOCs were based on the thin-film electrolytes;[83-85] however if this resistance showed no effect on the SOCs' functionality (for example, potentiometric-type sensors),[86] the traditional electrolyte-supported cells can be employed.

Table 3 summarizes some important properties of the ceramics such as strength, hardness, toughness.[56,89-91] Among them, the influence of pH_2O on the thermal behavior is most widely studied one. Moreover, thermal expansion played an important role in the applications of the electrolytes in the thin film mode. The match of thermal expansion coefficients (TEC) of SOCs' functional layers is necessary to ensure good adhesion between them and to avoid any cracking and delamination. The perovskite-structured proton-conducting materials (based on $MZrO_3$, $MCeO_3$ and

$LaM'O_3$, where M = Ca, Sr, Ba; M' = Sc, Y, Yb) exhibited TECs values between 8×10^{-6} and 12×10^{-6} K^{-1}, depending on the unit cell size and crystal symmetry. These TEC values were rather close to that of the traditional oxygen-conducting YSZ ($10\text{-}11\times10^{-6}$ K^{-1}).[92] The unique feature of the relative dimensions' change consisted in its nonmonotonicity due to the chemomechanical response (**Figure 7**).[47,102] Figure 7a schematically demonstrated the influence of the pH_2O-induced chemical expansion on the total (measured) expansion of the proton-conducting materials. The following assumptions were considered: the dilatometry dependence was obtained under cooling mode in a wet atmosphere, from a high temperature (~1000 °C), when a proton conductor was almost (fully) dehydrated. A linear shrinkage or contraction of the sample's dimension was accompanied with the decrease of the temperature. At lower temperatures, the available oxygen vacancies started to be filled with steam, initiating a chemical expansion. This chemical expansion was nonmonotonic with a continuous decrease in the temperature and reached a certain level, corresponding to the full hydration. The temperature dependence of relative change of linear parameters was characterized in different temperature regions, corresponding to different TEC values (**Table 4**).[44,49,93-103] Depending on modes of obtained data (cooling or heating), the initial condition of samples (hydrated or dehydrated) and the type of atmospheres (dry or wet), the different thermal expansion behaviors of materials can be achieved (Figure 7b and c).

3.1.6. Transport properties (conductivity, transport numbers)

The transport properties of the proton-conducting electrolytes based on $BaCeO_3$ or $BaZrO_3$ are very complex since their total conductivity is composed of six conductivities such as oxygen-ionic, protonic and electronic bulk conductivities and oxygen-ionic, protonic and electronic grain boundary conductivities. These conductivities depended on the internal characteristics of the materials

(composition, grain size, porosity) as well as the external characteristics (temperature and partial pressures of potential-determined components). In order to describe these processes more correctly, some special conditions can be constructed when conductivities dominated over others.

In polycrystalline materials,[20,104] the grain boundaries determined the overall transport of the considered electrolytes at lower temperatures, while the bulk region predominated at higher temperatures (**Figure 8**).[108] This behavior can be applied for massive ceramic samples and it should be considered when developing the electrolyte-supported electrochemical devices operated at higher temperatures. However, the grain boundary transport displayed a significant impact on the output of low- and intermediate temperature SOCs, if they are based on nanocrystalline thin film materials. From the macroscopic viewpoint, the grain boundary resistance of the electrolytes can be reduced by increasing the grain size or decreasing the grain boundary density. There are two well-known strategies to facilitate the grain growth such as the use of nanosized materials with enhanced sinterability[81,105] or the addition of sintering additives.[106,107] Both of these methods are useful for developing high-efficient electrochemical devices.

Temperature and chemical compositions of the materials and surrounding gas atmosphere determined the individual conductivity, which can be attributed to the bulk transport at temperatures higher than 500-600 °C. According to the profiles of defect concentrations under different conditions (Figure 2), the corresponding individual conductivity may predominate under a certain condition (**Figure 9**):[109]

1. Protonic conductivity predominated under atmospheres with high pH_2O and low pO_2 levels (wet N_2, wet H_2) at intermediate temperatures.

2. Oxygen-ionic conductivity predominated under dry reducing atmospheres (dry N_2, dry H_2, dry NH_3), especially at high temperatures.

3. Hole conductivity predominated in dry oxidizing conditions at elevated temperatures.

In the $BaCe_{1-x-y}Zr_xM_yO_{3-\delta}$ system, overall proton transport diminished with increasing Zr concentration (x), which can be explained by a pivotal role of grain boundaries for the Zr-enriched ceramic materials; at the same time, p-type electronic transport starts to be a dominant factor under oxidizing atmospheres.[37,40,110] As for the effect of M^{3+} acceptor dopants, a high ionic transport was observed for dopants with low ionic radii (M = Yb, Y, Dy, Ho) with their concentrations around 0.2.[111-115] An increase in the ionic radius of M was accompanied with the increasing Zr amount with reduced grain growth rate and grain boundary conductivity as well as an improved electronic transport capability.

In addition to the perovskites based on $BaCeO_3$ and $BaZrO_3$, the partial substitution of Ba^{2+} with other alkaline-earth elements might be useful to extend the electrolytic domain boundaries. Early studies have shown that Ca- or Sr-substituted barium cerate electrolytes demonstrated a higher proton transport number compared with the materials without such a modification[116-118], which implied a proton transport improvement. Moreover, the chemical stability improved slightly for the Ca- or Sr-substituted materials due to the decreased basicity of these ions. As a result, joint modification of both A- and B-sublattices in $Ba(Ce,Zr)O_3$ has been successfully used to from new highly stable electrolytes with predominant proton conductivity in the past few years.[119-125]

Among proton-conducting SOCs, fuel cells and electrolysis cells are widely investigated. In SOFCs and SOECs, the electrolyte is in contact with both oxidizing and reducing atmospheres. These

electrolyte membranes were almost protonic in wet H_2, while undesirable electron conductivity appeared in oxidizing conditions (e.g., static air, one of the most used atmosphere in SOFCs), even at 600 °C. The moisturizing of air led to a decrease in the absolute value and contribution of electron conductivity in the overall conductivity, as shown in the analysis of transport numbers distribution (Figure 9).

3.2. Air electrodes

The development of air (oxygen) electrodes plays a highly important role because the rapid development of SOCs based on thin-film electrolytes and their insufficient electrochemical activity at lower operational temperatures (<600 °C).[126,127] The air electrodes should also have good, chemical and thermal compatibility with other cell components as well as microstructural stability during the thermal cycles or long-term operation. For the proton-conducting SOCs, the stability of air electrodes in highly humid atmospheres is also required.

The same electrode exhibited different electrochemical activities when they were fabricated on the oxygen-ionic and proton-conducting electrolytes, which came from the distinctive elementary reactions realized in the electrode/electrolyte systems as shown in **Table 5** and **Figure 10**.[128,129] From the viewpoint of overall electrochemical reactions, equation (13) and (14) highlighted the above-mentioned differences of these systems:

$$\text{For } O^{2-}\text{electrolytes}: \quad O_2 + 2V_O^{\bullet\bullet} + 4e^{/} \rightleftarrows \qquad (13)$$

$$\text{For } H^{+}\text{electrolytes}: \quad O_2 + 4OH_O^{\bullet} + 4e^{/} \rightleftarrows \quad 2H_2O \qquad (14)$$

Two main factors affected the electrochemical activity of the air electrodes such as the kinetic parameters (diffusion coefficients and surface exchange constants) and the microstructural parameters (electrocatalytic active area). The parameters of the first group lie in the materials science aspect and can be managed by the selection and optimization of electrode compositions; the parameters of the second group can be controlled through the optimization of technological methods. Analysis on the relationship between the electrochemical activity, kinetic and microstructural parameters has been thoroughly carried out.[130–135] However, the influence of air humidification on the oxygen electrodes' performance was not clear, particularly for the proton-conducting SOCs.

One of the first investigations in this field was carried out by Grimaud et al.[136] They studied several oxygen electrode materials such as $La_{0.6}Sr_{0.4}Fe_{0.8}Co_{0.2}O_{3-\delta}$ (LSFC), $Ba_{0.5}Sr_{0.5}Co_{0.8}Fe_{0.2}O_{3-\delta}$ (BSCF), $PrBaCo_2O_{5+\delta}$ (PBC) and $Pr_2NiO_{4+\delta}$ (PN) fabricated on a proton-conducting $BaCe_{0.9}Y_{0.1}O_{3-\delta}$ electrolyte. These electrodes were divided into two groups by measuring the polarization resistances (R_p) with the dependence on pH_2O (**Figure 11**).[136] The first one included LSFC only, the electrochemical activity of which reduced with the increase in pH_2O. The second group consisted of other three oxygen electrodes, which showed increasing electrochemical activity with the increased pH_2O. In addition, the experimental data were analyzed using the following equation

$$R_p \propto (pO_2)^{-m}(pH_2O)^{-n} \qquad (15)$$

and the order coefficients (m and n) were determined. Considering the water vapor partial pressure behavior, n was found to be 1/2 for steps 7 and 8 and m was 1 for step 9 of Model II (Table 5) based on He et al.'s study.[137] For the PN electrode, the resistance at the medium and low frequencies was

proportional to pH_2O with n values of 1/2 and 1, respectively, demonstrating that the processes occurred with the participation of protons in both the interface and electrode's surface regions. The behaviors of BSCF and PBC were slightly different from that of PN, but their resistance showed the reverse tendency against pH_2O. However, LSFC exhibited a positive order of the resistance to pH_2O at medium frequencies and no order at low frequencies, suggesting its inability to hydration process. The rate determining step for LSFC was proposed to be oxygen adsorption/dissociation while for rate determining step for other three oxygen electrodes was water formation or steam releasing process.

Yoo et al. have studied the effect of the electrolyte material addition ($BaCe_{0.9}Y_{0.1}O_{3-\delta}$) to the LSFC oxygen electrode to enhance its electrochemical activity.[138] It was found that an increase of pH_2O led to an increase in the R_p values for both single-phase and composite electrodes. However, the absolute R_p values for the composite material in dry and wet atmospheres were lower than those of the single-phase one, suggesting the extension of the triple phase boundary (TPB) area by adding the electrolyte material.

Double perovskites with $PrBaCo_{2-x}Fe_xO_{5+\delta}$ compositions (x = 0, 0.5, 1 and 1.5) have been proposed as potential air electrodes for proton-conducting SOCs.[139] The pure Co-based and Fe-enriched electrodes demonstrated different electrodes' behaviors with the pH_2O variation. The R_p value of PBC decreased from 0.60 to 0.38 Ω cm^{-2} with an increase of pH_2O from 0.03 to 0.30 atm (600 °C), whereas it increased from 8.1 to 8.5 Ω cm^{-2} for $PrBaCo_{0.5}Fe_{1.5}O_{5+\delta}$ when pH_2O was increased from 0.03 to 0.30 atm at 600 °C. The obtained results were explained by the unique hydration capability of the Fe-free cobaltite with triple-conducting behavior, at which all the electrode surface participated in the electrode processes. The Fe-doped double perovskite showed a less pronounced tendency to hydration and, therefore, it demonstrated predominantly O^{2-}/electron mixed

conducting capability. In this case, the water formation (equation (14)) was proposed to be happened only over the electrolyte surface, impeding the competed oxygen transfer through the electrolyte/electrode interface.

The recently published work of Zohourian et al. demonstrated some directly opposite results.[140] The authors studied the proton uptake capability of ~20 simple perovskite oxides belonging to ferrite or cobaltite family (**Figure 12**).[140] They found that the hydrogen content was determined by the basicity of cations in ABO_3 and covalent character of B–O bonds, reaching the highest values for barium ferrites doped with lanthanum and zinc, respectively. However, the Co-containing oxides showed the lowest values. For example, the hydration enthalpy and entropy parameters of $Ba_{0.95}La_{0.05}Fe_{0.8}Zn_{0.2}O_{2.4}$ were −86±5 kJ mol^{-1} and −134±6 J mol^{-1} K^{-1}, respectively, allowing the uttermost protons concentration (10 mol.%) to be achieved in the oxide structure. These results open a possibility for searching the new and effective triple-conducting electrodes instead of cobaltites with simple or double perovskite structures,[141,142] for some of which the proton transfer was assumed to be questionable.[143] Some other double perovskites were also studied by Strandbakke et al.[128] $BaGd_{0.8}La_{0.2}Co_2O_{6-\delta}$ demonstrated a hydration capability with the corresponding enthalpy and entropy parameters of −50(±7) kJ mol^{-1} and −140(±10) J mol^{-1} K^{-1}, respectively. This oxygen electrode displayed different responses on the humidification extents of the atmospheres. At 650 °C, its R_p value increased when the pH_2O was changed from 0.002 to 0.014 atm while a reverse tendency was observed at 400 °C with a pH_2O change from 5×10^{-5} to 0.027 atm. Protons were not participated directly in the electrode process at higher temperatures, which contributed to the slow rates for oxygen adsorption/diffusion due to the less available active sites for oxygen transfer. On the other hand, at low temperatures, when both the electrolyte and

electrode were hydrated, the protons determined the electrode process through the stage 7 of Model III (Table 5).

Sun and Cheng have studied the BSCF|BCZYYb|BSCF symmetrical cells to reveal the behaviors of the electrolyte and the electrodes in dry (10^{-6} atm) and wet (0.03, 0.1 and 0.2 atm) air atmospheres at 450, 550 and 650 °C.[144] It was found that the R_o decreased with the increase in the pH_2O level and then kept constant until the hydration limit. For example, the R_o values were 2.11, 2.04, 1.96 and 1.94 Ω cm^2 at 10^{-6}, 0.03, 0.1 and 0.2 atm of pH_2O (650 °C), respectively; they were around 6 Ω cm^2 at all the atmospheres with different pH_2O levels at 450 °C. It indicated that the proton-conducting behavior of the BCZYYb electrolyte was dominated by the proton transport at low temperatures. In contrast to R_o, the R_p value increased with increased water concentrations at all temperatures. The detailed analysis of electrochemical impedance spectroscopy (EIS) data (**Figure 13**) was used to conclude that the electrochemical activity deterioration was associated with an increased resistance at medium and low frequencies and a slight decrease in the resistance at high frequency.[144] These resistances can be assigned to the mass transport of oxygen molecules, oxygen adsorption/dissociation and the charge transfer processes at low, medium and high frequencies, respectively. The presence of H_2O in air resulted in its adsorption on the electrolyte and electrode surfaces, which decreased the amount of active sites for oxygen adsorption, dissociation and transport. The dominance of proton transfer was confirmed by the lower resistance of the high frequency process responsible for the total charge transfer of the electrode reactions. Moreover, the effect of CO_2 poisoning on the electrochemical properties of the symmetrical cells was also investigated and it was found that BSCF was unstable in CO_2, especially at low temperatures (450

and 550 °C). However, its stability was enhanced partially by moisturizing of the CO_2-containing atmosphere due to the decreased active sites for CO_2 adsorption by the addition of steam.

The BSCF electrode was also compared with other oxygen electrodes such as Ag, LSFC and LSFC–BCZYYb.[129] The authors performed the experiments in the same condition (T = 450–650 °C, $pH_2O = 5\times10^{-6}$, 0.03–0.30 atm) and proposed possible mechanisms for all the four electrodes (Figure 10). It was found that both Ag and LSFC materials were unsuitable as effective single-phase electrodes due to shorter TPB length. The addition of BCZYYb to LSFC phase resulted in an extension of TPB area. BSCF was identified as the more suitable oxygen electrode for proton-conducting SOCs owing to lowest R_p values in both dry and wet atmospheres (**Figure 14**).[129]

Along with materials with the perovskite-related structures, the complex oxides belonging to the Ruddlesden-Popper phases are also considered as attractive electrodes for protonic-conducting electrolytes in SOCs. For example, the $Ln_2NiO_{4+\delta}$-based materials (Ln = La, Pr, Nd) exhibit hydration capability,[145] high chemical stability against the hydroxide and carbonate formation due to the absence (or reduced amount) of alkaline-earth elements [146,147], quite low TEC values close to those of electrolytes,[148,149] no meaningful pO_2-induced chemical expansion,[150,151] high electrical conductivity,[152,153] and excellent electrochemical activity as a result of both high oxygen diffusion coefficients and surface exchange constants.[154,155]

Table 6 summarizes the R_p values of the various oxygen electrodes based on symmetrical cells in various atmospheres with different water concentrations.[128,136-139,144,156-158] As can be seen, some opposite tendencies were found even for the same electrode. Different reasons may contribute to the observed disagreement, which will be mentioned later. Firstly, in Table 5,

the proposed models were based on the fact of unipolar (oxygen ionic in dry atmospheres or protonic in wet atmospheres) transport in the electrolytes. However, the $BaCeO_3$ and $BaZrO_3$-based materials exhibited substantial electron transport in oxidizing conditions even at 600 °C.[44] Secondly, these electrolytes demonstrated co-ionic (oxygen-ionic + protonic) conductivity in a wide temperature range (550-750 °C), which resulted in the water formation (equation (14)) as well as oxygen reduction (equation (13)) reactions simultaneously. Finally, the microstructural parameters of electrodes (tortuosity, porosity, type and size of grains) were not considered in the proposed models and investigations, which also played important roles in controlling the kinetic parameters and the electrochemical activity.

3.3. Fuel electrodes

Fuel electrodes of proton-conducting SOCs, which are similar to the traditional oxygen-conducting SOCs, should meet several requirements such as high electronic conductivity and sufficient ionic conductivity to ensure electro-catalytic activity for fuel oxidation; chemical inert to the interactions with gas components of fuels (H_2, CO, CO_2, H_2S) and other components of SOCs; thermal compatibility with cell components; structural and mechanical flexibility between oxidizing and reducing atmospheres (redox-stability).[159–162]

The composite materials composed of a metal (typically nickel) and ceramic components (electrolyte material) are traditional fuel electrodes for proton-conducting SOCs by meeting the above-mentioned requirements. A Ni-metallic phase provides electron transport, whereas ionic (protonic) transport was provided by the ceramic part. The optimized ratio of phases and content of pore

former during materials preparation ensured the mechanical and redox stability of Ni-based cermets. The use of the same material for both the ceramic component of cermets and the electrolyte resulted in excellent compatibility of the cell components.

The existing works aimed to the optimization of microstructural, stability, electrical and electrochemical properties of the composite anodes for proton-conducting SOFCs and SOECs by controlling the ratios of the electrode components.[163–169] For example, Nasani et al. fabricated the symmetrical cells based on the $BaZr_{0.85}Y_{0.15}O_{3-\delta}$ (BZY15) electrolyte and Ni–BZY15 anode and studied their electrochemical activity in reducing atmospheres with different pH_2 and pH_2O values.[170] They found that the R_p values decreased with increasing pH_2 (from 0.001 to 0.1 atm) and were unchanged with increasing pH_2O (from 6×10^{-4} to 0.03 atm in 10 vol.% H_2/N_2). Based on the comparative analysis, it can be concluded that dissociative adsorption of hydrogen on the anode surface was a rate-determining step ($H_{2(gas)} \rightleftarrows$ rface), which was not dependent on the pH_2O variation.

Miyazaki et al. have studied the electrochemical behavior of a proton-conducting SOFC fueled with NH_3.[171] Pure oxygen and NH_3+Ar+H_2O mixtures were used as the cathodic and anodic atmospheres for the cell with a configuration of Ni–$BaZr_{0.8}Y_{0.2}O_{3-\delta}$ (BZY20)|BZY20|Pt. It was found that the total polarization of the electrodes decreased from 0.99 to 0.86 Ω cm^2 at 650 °C with a pH_2O increase from 0 to 0.2 atm due to the change in the rate-determining step. The ammonia decomposition was found to be determining factor for the dry fuel, whereas the hydrogen oxidation reaction dominated in the wet fuel.

Ding et al. fabricated the symmetrical cells made of $Ba_2FeMoO_{6-\delta}$ (BFM)|BCZYYb|BFM and studied the electrochemical activity of the fuel electrodes.[172] Mo-based double perovskites have

attracted more and more attention due to their good mixed ionic-electronic conductivity, mechanical stability and acceptable expansion behavior with various temperatures and pO_2 values.[173–176] Moreover, it was found that these oxides (e.g., $Sr_2Fe_{1.5}Mo_{0.5}O_{6-\delta}$) may have high bulk proton transport,[177,178] which was favorable for proton-conducting SOCs. In Ding et al.'s work, the BFM electrodes were prepared by solid state reaction (SSR) and Pechini methods.[172] The EIS data showed that electrodes prepared by Pechini method exhibited higher electrochemical activity than that prepared by SSR. BFM prepared by SSR method displayed ASRs of ~250, 70, 30 and 10 Ω cm^2 at 600, 650, 700 and 750 °C, respectively (dry 5 vol.% H_2/Ar). Moisturizing of an H_2/Ar by 3 vol.% water vapor resulted in an ASR decrease to ~85, 25, 10 and 6 Ω cm^2 at corresponding temperatures. It suggested that the rate-limiting step was the proton-charge transfer for BFM prepared by SSR method while hydrogen dissociation and diffusion was the rate-limiting step for BFM prepared by the Pechini method. However, the obtained data were not sufficient to explain the pH_2O influence on considerable improvement of electrode activity, which needed to be clarified in the future research.

4. Functional materials of proton-conducting SOCs

The electrochemical cells with potential-determined components working under the high partial pressure differences represent model systems closest to real conditions of SOFCs and SOECs. From the viewpoint of thermodynamics, such cells in non-current mode can generate a voltage (open circuit voltage, OCV), which is determined by transport nature of electrolytes and created gradients:[179,180]

$$E = t_O \frac{RT}{nF} \ln \frac{p'O_2}{p''O_2} + t_H \frac{RT}{nF} \ln \frac{p''H_2}{p'H_2} = t_O E_O + t_H E_H \quad (16)$$

where E_O and E_H are the thermodynamic values of oxygen and hydrogen concentration cells under created partial pressure differences of oxygen ($p'O_2$, $p''O_2$) and hydrogen ($p'H_2$, $p''H_2$), t_O and t_H are the oxygen-ionic and protonic transport numbers. Considering the equilibrium of $H_2O \rightleftarrows H_2 + 1/2O_2$ reaction, equation (16) is equivalent to the following expression:

$$E = t_i \frac{RT}{nF} \ln \frac{p'O_2}{p''O_2} + t_H \frac{RT}{nF} \ln \frac{p''H_2O}{p'H_2O} = t_i E_O + t_H E_{H_2O} \quad (17)$$

where E_{H_2O} is the thermodynamic value of water vapor concentration cell under created difference of water vapor pressures ($p'H_2O$, $p''H_2O$); $t_i = t_O + t_H$, which is the total ions transport numbers.

As can be seen from equation (17), proton-conducting SOCs are more efficient than oxygen-ion-conducting SOCs because of the higher OCV values for SOFCs and lower OCV values for SOECs due to the additional component ($t_H E_{H_2O}$). Nevertheless, even if the pH_2O levels are the same between the opposite sides of an electrolyte membrane, the proton-conducting SOCs systems might be preferable than oxygen-ionic-conducting analogs.[181-183] A possible improvement comes from not only tailoring OCVs (and, correspondingly, efficiency of SOCs) on account of higher t_H, but the higher conductivity of the electrolyte membranes (and, correspondingly, performance of SOC). The above analysis demonstrated a great importance of setting and controlling the water vapor partial pressures in both gas sides of SOCs.

4.1. SOFCs

4.1.1. The electrolyte-supported configuration

One of the first studies concerning the SOFC's characterization at different moisturizing contents of gases has been carried out by Taherparvar et al.[184] The authors fabricated the electrolyte-supported Pt|$SrCe_{0.95}Yb_{0.05}O_{3-\delta}$ (SCY)|Pt cell and characterized it at 600, 700 and 800 °C in the fuel cell mode, varying the pH_2O level (from 0.001 to 0.12 atm) in oxidizing and reducing atmospheres. When pH_2O was increased in air atmosphere (pH_2O = 0.03 in a fuel mixture of 10 vol.% H_2/Ar), the peak power densities (PPDs) decreased from 2.14 to 1.73 mW cm^{-2} at 600 °C and 7.70 to 6.53 mW cm^{-2} at 800 °C, although the total cell resistance was unchanged with humidification. The deterioration of cell performance was associated with a decrease of OCVs (from 1.113 to 0.993 V at 600 °C and from 0.95 to 0.91 V at 800 °C), which showed the same tendency to the theoretical values with increasing pH_2O value. When pH_2O was increased in 10 vol.% H_2/Ar atmosphere from 0.001 to 0.03 atm (pH_2O in the air was about 0.001 atm), the PPD of the fuel cell increased from 2.67 to 3.56 mW cm^{-2} at 700 °C with a decrease of the total cell resistance from 100 to 75 Ω cm^2. The authors concluded that hydrogen humidification was more efficient to obtain high performance than the air humidification. However, some controversies were also found by analyzing the electrical properties of the SCY electrolyte. Both electronic and ionic conductivities of SCY were found to be decreased significantly with an increase in pH_2O; therefore, the total cell resistance should be increased at air humidification as well as hydrogen humidification, which was not observed experimentally.

4.1.2. The electrode-supported configuration

He et al. developed an anode-supported SOFC of Ni–$BaCe_{0.5}Zr_{0.3}Y_{0.2}O_{3-\delta}$ (BCZY0.3)|BCZY0.3|$Sm_{0.5}Sr_{0.5}CoO_{3-\delta}$ (SSC)–BCZY0.3 with 20 µm-thick electrolyte and studied the

correlations between cell performance and the variation of pH_2O levels in the cathode chamber at 700 °C (**Table 7**).[185] Based on the analysis of EIS spectra with a $R_O(R_HQ_H)(R_LQ_L)$ equivalent circuit (**Figure 15**),[185] the rate-limiting process was associated with the cathode reactions, including proton migration (step 7 of Model II , Table 5) and oxygen-ion migration (steps 5 and 6 of Model II) to the TPB. An increase of pH_2O resulted in an increased R_p value due to their low frequency contributions. It indicated that adsorption stages as well as diffusion of gas components to TPB started to be rate-limiting processes at high pH_2O values.

The influence of the pH_2O in oxidizing and reducing atmospheres on the performance of SOFCs based on Ni-$BaCe_{0.85}Y_{0.15}O_{3-\delta}$ (BCY15)|BCY15|$La_{0.8}Sr_{0.2}MnO_{3-\delta}$ (LSM) with a 20 μm-thick electrolyte has been studied at 700 °C using a distribution relaxation time (DRT) and EIS analyses.[186] It was found that the increasing pH_2O level at the anode side from 1×10^{-4} to 0.071 atm (pH_2O = 1×10^{-4} atm in the cathode side) led to the some changes in the cell performance. For example, PPD was changed from 210 to 200 mW cm^2, OCV was reduced from 1.05 to 1.02 V and the R_p was changed from 0.95 to 1.17 Ω cm^2 with almost unchanged R_o value. The EIS spectra were fitted using a L-$R_O(R_1Q_1)(R_2Q_2)(R_3Q_3)$ equivalent circuit and then were analyzed by separating the individual processes such as P_1, P_2 and P_3 with corresponding resistances (R_1, R_2 and R_3, respectively). Based on this analysis, some important conclusions were identified. Firstly, R_1 decreased slightly with the pH_2O change from 1×10^{-4} to 0.023 atm and then it kept constant with further increased humidification content. R_2 was almost constant, whereas R_3 increased from 0.08 to 0.30 Ω cm^2 with the pH_2O change from 1×10^{-4} to 0.023 atm. According to these qualitative and quantitative data, the P_1 process was attributed to the charge exchange behavior, which was enhanced by the humidification due to the fast proton transport in comparison with oxygen-ionic one; the P_3 process corresponded

to gas diffusion processes in the pores of the electrode because increased concentration of pH_2O hindered the H_2 supply to the electrochemical active zone.

The effect of humidification amounts of the cathodic atmospheres on the cell performance was also investigated.[187] For example, when pH_2O was increased from 1×10^{-4} to 0.071 atm, the PPD decreased from 170 to 140 mW cm^2 due to the increased R_o value from 0.60 to 0.75 Ω cm^2, R_2 value from 0.66 to 1.07 Ω cm^2, R_3 value from 0.12 to 0.21 Ω cm^2 while no inhibition of the transfer process of charge carriers (P_1 process) was observed. In addition, the stages associated with the hindrance of the water desorption (P_2 process, equation (14)) and oxygen adsorption (P_3 process, equation (13)) were also limited. The above results suggested that cathode material with low ionic conductivity such as LSM was not suitable as air electrode for proton-conducting SOCs.

Lee et al. demonstrated that transport properties of air electrodes strongly affected the SOFCs' performance under humidification.[187] It was found that the total cell resistances increased for both cells of Ni-BCY15|BCY15|LSM-$Ce_{0.8}Sm_{0.2}O_{2-\delta}$ (SDC) and Ni-BCY15|BCY15|LSM-BCY15, when dry air and dry hydrogen atmospheres were replaced by wet ones with pH_2O = 0.03 atm. However, the R_p for the composite material with proton-conducting component (LSM-BCY15) showed less performance deterioration than for the composite electrode containing oxygen-conducting part (LSM-SDC).

Lim et al. prepared SOFCs with a more stable $BaCe_{0.45}Zr_{0.4}Y_{0.15}O_{3-\delta}$ as the electrolyte (BCZY0.40, 15.5 μm in thickness).[188] They also replaced the LSM cathode with mixed ionic-electron conducting BSCF, which showed improved activity and hydration capability due to mixed conductivity. As shown in **Figure 16**, the air moisturizing resulted in the considerable drop in PPD

(from 0.80 to 0.46 W cm^2) due to the increase in R_2 and R_3 resistances assigned to the proton transfer through the electrode/electrolyte interface and oxygen surface exchange between the electrode's surface and gas atmosphere, respectively.[188]

Pikalova and Medvedev studied the effect of hydrogen humidification on the performance of the fuel cell with a configuration of Ni-$BaCe_{0.89}Gd_{0.1}Cu_{0.01}O_{3-\delta}$ (BCGC)|BCGC|Pt at 600 and 750 °C to determine the transport nature of the BCGC electrolyte.[189] An increase in pH_2O at anode side showed a positive effect on the SOFC's efficiency due to the increased maximal voltage value (equation (17)). The electrochemical system was modified by an additional oxygen sensor, which was used to monitor the oxygen partial pressure difference to estimate the thermodynamic E_O level. Such a cell demonstrated higher OCV values than E_O at high concentration of water vapor in hydrogen. This kind of result was obtained for the first time for electrode-supported configuration, indicating the predominance of proton transport of BCGC at 600 °C and co-ionic transport at 750 °C (**Figure 17**).[189] The separation of R_o and R_p from the total cell's resistance was carried out by using a current interruption method. The R_o value was found to be constant with the pH_2O variation while the R_p increased with an increase in pH_2O. Although the authors proposed that this phenomena was due to the increased overpotential of the oxygen electrode, the inhibition of the rate-limiting reactions at the anode side also had some contributions, including ionization of adsorbed hydrogen in nickel surface and its charge transfer trough the Ni/BCGC interface.[190]

Danilov et al. studied the effect of simultaneous moisturizing of gases on the performance of Ni-$BaCe_{0.5}Zr_{0.3}Dy_{0.2}O_{3-\delta}$ (BCZD)|BCZD|$YBaCo_{3.5}Zn_{0.5}O_{7+\delta}$ (YBCZ) cell operating in the fuel cell mode.[191] **Table 8** summarizes the main characteristics of the fuel cell when the pH_2O value was increased from 0.03 to 0.10 atm in both anodic and cathodic atmospheres.[191] The film conductivity and the

ion transport numbers of the BCZD electrolyte increased with the increased moisturizing extent. However, the PPD showed a reverse tendency owing to the deterioration of the electrochemical activity of the electrode (resistance increased by 2 times). The inhibition of oxygen-related processes due to the surface adsorption of the water vapor at the cathode side was proposed to be the main factor resulting in an increased electrode overpotential.

4.2. SOECs

The reverse operation of proton-conducting SOFCs is an electrolysis mode (SOECs), providing the electrochemical decomposition of steam at the anode (air) side, electrochemical permeation of protons through a dense electrolyte and hydrogen production (2 in Figure 1) or compounds reduction (3 and 4 in Figure 1) at the cathode (fuel) side. As shown in **Figure 18**, the R_p of the electrolysis mode decreased considerably as compared with the fuel cell mode.[185,193] He et al. proposed another reaction mechanism (equation (18)–(25)),[185] which was different from those presented in Table 5.

$$H_2O_{(g)} \rightleftarrows \quad (18)$$

$$H_2O_{ads} \rightleftarrows + H^+_{ads} \quad (19)$$

$$OH^-_{ads} \rightleftarrows H^+_{ads} \quad (20)$$

$$O^{2-}_{ads} - e^{/} \rightleftarrows \quad (21)$$

$$O^-_{ads} - e^{/} \rightleftarrows \quad (22)$$

$$2O_{ads} \rightleftarrows \quad (23)$$

$H^{+}_{ads} \rightleftarrows$ (24)

$H^{+}_{(tpb)} \rightleftarrows$ (25)

These reactions included the surface dissociative adsorption of water, oxygen charge transfer, formation and desorption as well as proton migration to TPB. It was found that the surface diffusion of adsorbed oxygen ions was not the rate-limiting step for electrolysis mode (as compared with fuel cell mode), whereas water ionization and proton transfer from the electrode surface to the electrolyte were found to be the rate-limiting steps in the electrolysis mode. An increased pH_2O in the air led to a decrease of R_p (Figure 18c) due to the promotion of these reactions and the enhancement of the charge transfer. The similar correlation between R_{total} and pH_2O at the anode side was also revealed by Azimova and McIntosh for the Ni-$BaCe_{0.48}Zr_{0.4}Yb_{0.1}Co_{0.02}O_{3-\delta}$ (BCZYC)|BCZYC|BCZYC–$La_{0.8}Sr_{0.2}CoO_{3-\delta}$ (LSC) electrolysis cell.[154]

Danilov et al.[194] have utilized a Ruddlesden-Popper $Nd_{1.95}Ba_{0.05}NiO_{4+\delta}$ (NBN) nickelate material in an electrolysis cell with a configuration of Ni-BCZD|BCZD (15 μm)|NBN. It was revealed that at 750 °C and thremoneutral mode (U ≈ 1.3 V) the current density values increased from 665 to 810 mA cm^{-2} when pH_2O in air was changed from 0.03 to 0.50 atm. This result was attributed to behavior of the BCZD electrolyte (protonic conductivity increased and polarization resistance decreased from 0.55 to 0.51 Ω cm^2) as well as with a positive response of the NBN oxygen electrode (its polarization resistance varied from 0.05 to 0.03 Ω cm^2, respectively). According to the data obtained, NBN can be considered as an active electrode toward reaction (14) due to its possible hydration capability revealed for similar nickelates.[136]

Zhu et al.[195,196] carried out the mathematical modeling of SOCs based on proton-conducting electrolytes by means of a Nernst-Planck model and established effects of air humidification and electron conductivity on the performance and efficiency of SOCs operated in both fuel cell and electrolysis cell modes as shown in **Figure 19**.[195,196] According to their data, the air humidification slightly affected the cell performance (the total polarization was assumed to be constant) for both modes, however, considerably improved their efficiency. The efficiency increased with diminishing pO_2, which was determined by the p-type electronic conductivity of the electrolytes as shown in equation (4). Based on Figure 19, it showed that Ce-enriched membranes were more preferable than Zr-enriched ones for utilization in highly humid atmospheres; however, the poor chemical stability of Ce-enriched materials limited their widespread use, especially for low-temperature ranges.

5. Long-term stability and degradation phenomena

Decreasing the operation temperatures of SOCs is required to impede the rate and degree of degradation processes and to extend the lifetime of the electrochemical devices. However, their operation at the intermediate- and low-temperature ranges also suffered from the degradation phenomena due to the different chemical and physical processes.[133,197-201] For example, some changes occurred as for the individual functional materials (grain aging, coarsening, recrystallization, cracking and material decomposition) as well as for the corresponding interfaces (phase interaction, cation segregation and delamination).

Considering the proton-conducting SOCs, the low chemical stability of the electrolyte materials at a high concentration of H_2O and CO_2 and their expansion incompatibility with other

functional materials can be considered as ones of the main reasons leading to the degradation. A negative effect of CO_2 on both electrolyte and electrode resistances of the BSCF|BCZYYb|BSCF symmetrical cell was reported.[144] The cells were treated in an atmosphere with 1% CO_2 at 450, 550 and 650 °C for 2 h, characterized by EIS analysis before and after the CO_2 treatment. It was found that the maximal degradation degree (DD) of the R_o was ~8% after the CO_2 treatment. At the same time, the deterioration degree of R_p was much higher by 50-110%, which, however, decreased down to ~65% after the recovery procedure as compared with the initial values. Chemical instability of the electrolyte in H_2O-enriched atmospheres was observed for $BaCe_{0.8}Zr_{0.2}O_{3-\delta}$ (BCZ).[202] The cells with a ~15 μm electrolyte were characterized in the electrolysis mode. For the cell with BCZ electrolyte, the DD level for current density (U = 1.1 V) was 9%, whereas DD for the total resistance (caused by the increase of ohmic contribution) was ~7% after 10 hours' operation. Li et al. fabricated and characterized a SOEC cell with 15 μm-thick $BaCe_{0.5}Zr_{0.3}Y_{0.16}Zn_{0.04}O_{3-\delta}$ electrolyte in short-time mode (10 h).[203] During this period, the DD level for current density and total cell's resistance were 12 and 15%, respectively.

The degradation degree seems to be higher under the electrolysis mode than the fuel cell mode. Ye et al. have studied a SOC with $CaZr_{0.9}In_{0.1}O_{3-\delta}$ electrolyte under reversible operation.[204] The DD values for current density and total resistance were 18 and 12% after 8 hours' electrolysis process, respectively (U = 1.2 V, 850 °C). On the other hand, no changes in current density (U = 0.8 V, 850 °C) were observed in the fuel cell mode. The authors considered that the degradation process in SOEC mode was attributed to the change in anode microstructure resulted from nickel coarsening at high operational temperatures. However, it was unclear why such a coarsening behavior did not result in a cell performance degradation in the fuel cell mode. Most probably, the bias potential

applied to SOCs affected the degradation parameters, since the same electrode was polarized differently, causing the occurrence of some unequal elementary reactions (refer to the comparison between Table 5 and equation (18)–(25)). The degradation of the R_o in the electrolysis mode was found by Bi and Traversa even for a highly stable proton-conducting electrolyte ($BaZr_{0.8}Y_{0.2}O_{3-\delta}$, BZY).[205] They observed an increase of the R_o from ~8.47 to 8.58 Ω cm^2 after 80 h of operation (fuel atmosphere = 5 vol.% H_2/Ar, oxygen atmosphere = 3 vol.% H_2O/air, U = 1.3 V). Since no chemical interaction between BZY and H_2O was predicted, such an ohmic deterioration can be assigned to the chemical expansion behavior of the electrolyte due to the continuous steam supply to the electrode/electrolyte interface in the electrolysis mode. A temperature of 600 °C was suitable for gradual hydration of BZY with chemical expansion effects (Figure 5 and Figure 6) and a strain and stress between the functional materials were observed.

6. Conclusions and perspectives

The oxides with proton-conducting capability are interesting and highly promising materials for various electrochemical applications, including SOFCs and SOECs, pumps and sensors, reactors and converters. Protons are formed through their interaction of oxide materials with the hydrogen-containing component in the gas atmospheres at elevated temperatures. This process occurs generally through the filling of oxygen vacancies existed in the oxides by water vapor, which is determined by the inherent properties of the materials (cell components) and two external factors (temperature and water vapor partial pressure), which can be easily set and controlled.

The appearance of protons induced the structural changes, affecting the pH_2O-determined functional properties differently (**Figure 20**). Proton charge carriers exhibited a very high mobility and a low migration barrier. This allows a higher conductivity to be reached for the proton-conducting electrolytes, extending the operation range of electrochemical devices down to extremely low temperatures (300-500 °C).[83,142,206] Although undeniable advantages in ionic transport are observed for such electrolytes, there are a number of drawbacks, which might be the limiting factors for practical applications. Firstly, hydration process was accompanied by a mechanical stress appeared in electrolyte ceramics due to a pH_2O-induced chemical expansion, which was more pronounced for low- and intermediate-temperature ranges. Secondly, some electrolytes (highly conductive cerates) showed a low thermodynamic stability under humidified conditions, especially at temperatures below 600 °C. Therefore, a rational design of proton-conducting electrolytes should be carried out to improve the stability, mitigate pH_2O-induced chemical strain and maintain high ionic (including protonic) conductivity.

Regarding the electrode systems, they exhibited a low degree of hydration capability, although a relatively high concentration of protons has been revealed recently in the Zn-doped $BaFeO_3$ perovskite system.[140] The oxygen-ionic and electronic conductivity of Zn-doped $BaFeO_3$ allows developing new triple-conducting electrodes with promising electrochemical activity as a result of extending the electrochemical active area. In addition, barium ferrite based electrodes have been successfully examined experimentally in electrochemical cells with proton-conducting electrolytes.[207-209] It should be taken into account that most of the electrode materials demonstrated a undesirable pO_2-induced chemical expansion behavior due to the presence of Fe- and Co-ions with easy oxidation capability and spin state variations. This might be a significant

problem for joint application of electrolyte and electrode systems in the conditions of the thermo-cycles or simultaneous pO_2 and pH_2O variations. A possible solution to suppress the chemical expansion effect is the use of Fe- and Co-free electrodes, like oxides belonging to the Ruddlesden-Popper family. For some of them (e.g., $Ln_2NiO_{4+\delta}$), the hydration capability is also mentioned.[136] Moreover, the layered nickelates compositions contain no (or low) concentration of alkaline-earth elements, which positively affects the chemical stability of the electrodes.

Apart from the properties of the individual materials, pH_2O affected the interfacial behavior, which determined the kinetic parameters of electrode processes. Based on the literature review, this effect may improve or deteriorate the electrochemical reaction rates, which were reflected in the corresponding polarization characteristics. The most likely explanation for different electrode behaviors lies in predominant ionic conductivity of the electrolytes (oxygen ionic conductivity at high temperatures, protonic conductivity at low temperatures and co-ionic at medium temperatures)[37] as well as conduction nature (mixed oxygen-ionic/electronic or triple protonic/oxygen-ionic/electronic) of the electrodes, which depend on temperature, pH_2O and pO_2 conditions and affect the proton transfer processes through the electrode/electrolyte interface.

Considering the intermediate-temperature SOFCs and SOECs, their performance (peak power density, hydrogen evolution rate) under gas humidification can be varied in the positive or negative directions depending on the electrode response, while the electrolytic properties are always improved. Moisturizing the oxidizing atmospheres is beneficial to suppress the p-type electron transport in the electrolytes, whereas moisturizing the reducing atmospheres increases the electromotive force (or OCV), which is determined by the water vapor potential difference. Both these ways allow the improvement of energy efficiency of the electrochemical devices.

The different effect of pH_2O on the characteristics of the materials and interfaces should be comprehensively considered, when designing and developing the electrochemical devices operated under highly moisturizing atmospheres or ambient gases when pH_2O is not a constant parameter.

This review highlights the main findings of the effect of pH_2O variations on the performance and properties of materials and interfaces at elevated temperatures based on proton-conducting SOCs. However, some extension of knowledge in this field is still needed to provide some useful guidelines, allowing the solid oxide electrochemical cells to be effectively operated during a long period of time without any degradation processes caused by the existence of steam at low and intermediate temperature range.

Acknowledgements

Zongping Shao and Wei Wang would like to thank the Australia Research Council for supporting the project under contract DP150104365 and DP160104835. Dmitry Medvedev is grateful to the Russian Science Foundation (grants no. 16-19-00104 and 18-73-00001) and the Council of the President of the Russian Federation (grant no. СП-161.2018.1).

Received: ((will be filled in by the editorial staff))
Revised: ((will be filled in by the editorial staff))
Published online: ((will be filled in by the editorial staff))

References

[1] N. Mahato, A. Banerjee, A. Gupta, S. Omar, K. Balani, *Prog. Mater. Sci.* **2015**, *72*, 141.

[2] Z. Gao, L. V. Mogni, E. C. Miller, J. G. Railsback, S. A. Barnett, *Energy Environ. Sci.* **2016**, *9*, 1602.

[3] Z. Shao, M. O. Tadé. *Intermediate-Temperature Solid Oxide Fuel Cells. Materials and Applications*, Springer-Verlag Berlin Heidelberg, **2016**.

[4] S. Y. Gómez, D. Hotza, *Renew. Sustain. Energy Rev.* **2016**, *61*, 155.

[5] J. Choi, M. Shin, B. Kim, J.-S. Park, *Int. J. Hydrogen Energy* **2017**, *42*, 13092.

[6] L. Bi, S. Boulfrad, E. Traversa, *Chem. Soc. Rev.* **2014**, *43*, 8255.

[7] S. Hossain, A. M. Abdalla, S. N. B. Jamain, J. H. Zaini, A. K. Azad, *Renew. Sustain. Energy Rev.* **2017**, *79*, 750.

[8] W. Deibert, M. E. Ivanova, S. Baumann, O. Guillon, W. A. Meulenberg, *J. Membr. Sci.* **2017**, *543*, 79.

[9] Z. Tao, L. Yan, J. Qiao, B. Wang, L. Zhang, J. Zhang, *Prog. Mater. Sci.* **2015**, *74*, 1.

[10] A. Vourros, V. Kyriakou, I. Garagounis, E. Vasileiou, M. Stoukides, *Solid State Ionics* **2017**, *306*, 76.

[11] S. H. Morejudo, R. Zanón, S. Escolástico, I. Yuste-Tirados, H. Malerød-Fjeld, P. K. Vestre, W. G. Coors, A. Martínez, T. Norby, J. M. Serra, C. Kjølseth, *Science* **2016**, *353*, 563.

[12] H. Malerød-Fjeld, D. Clark, I. Yuste-Tirados, R. Zanón, D. Catalán-Martinez, D. Beeaff, S. H. Morejudo, P. K. Vestre, T. Norby, R. Haugsrud, J. M. Serra, C. Kjølseth, *Nat. Energy* **2017**, *2*, 923

[13] S. S. Hashim, M. R. Somalu, K. S. Loh, S. Liu, W. Zhou, J. Sunarso, *Int. J. Hydrogen Energy* **2018**, *43*, 15281.

[14] E. Fabbri, L. Bi, D. Pergolesi, E. Traversa, *Adv. Mater.* **2012**, *24*, 195.

[15] L. Yang, S. Wang, K. Blinn, M. Liu, Z. Liu, Z. Cheng, M. Liu, *Science* **2009**, *326*, 126.

[16] F. A. Kroger. *The Chemistry of Imperfect Crystals*. North-Holland Publishing Co., Amsterdam, **1964**.

[17] S.-J. Song, E. D. Wachsman, S. E. Dorris, U. Balachandran, *Solid State Ionics* **2002**, *149*, 1.

[18] N. Bonanos, *Solid State Ionics* **2011**, *145*, 265.

[19] A. Løken, T. S. Bjørheim, R. Haugsrud, *J. Mater. Chem. A* **2015**, *3*, 23289.

[20] G. Gregori, R. Merkle, J. Maier, *Prog. Mater. Sci.* **2017**, *89*, 252.

[21] D. A. Medvedev, J. G. Lyagaeva, E. V. Gorbova, A. K. Demin, P. Tsiakaras, *Prog. Mater. Sci.* **2016**, *75*, 38.

[22] J. M. Polfus, T. S. Bjørheim, T. Norby, R. Bredesen, *J. Mater. Chem. A* **2016**, *4*, 7437.

[23] K. Leonard, Y.-S. Lee, Y. Okuyama, K. Miyazaki, H. Matsumoto, *Int. J. Hydrogen Energy* **2017**, *42*, 3926.

[24] D.-K. Lim, H.-N. Im, S.-J. Song, H.-I. Yoo, *Sci. Rep.* **2017**, *7*, 486.

[25] M. Oishi, S. Akoshima, K. Yashiro, K. Sato, J. Mizusaki, T. Kawada, *Solid State Ionics* **2009**, *180*, 127.

[26] S. Ricote, N. Bonanos, G. Caboche, *Solid State Ionics* **2009**, *180*, 990.

[27] K. Leonard, Y.-S. Lee, Y. Okuyama, K. Miyazaki, H. Matsumoto, *Int. J. Hydrogen Energy* **2017**, *42*, 3926.

[28] K. D. Kreuer, *Annu. Rev. Mater. Res.* **2003**, *33*, 333.

[29] F. Krug, T. Schober, T. Springer, *Solid State Ionics* **1995**, *81*, 111.

[30] F. Krug, T. Schober, *Solid State Ionics* **1996**, *92*, 297.

[31] A. S. Farlenkov, L. P. Putilov, M. V. Ananyev, E. P. Antonova, V. A. Eremin, A. Yu. Stroeva, E. A. Sherstobitova, V. I. Voronin, I. F. Berger, V. I. Tsidilkovski, V. P. Gorelov, *Solid State Ionics* **2017**, *306*, 126.

[32] Y. Okuyama, T. Kozai, T. Sakai, M. Matsuka, H. Matsumoto, *Electrochim. Acta* **2013**, *95*, 54.

[33] Y. Okuyama, T. Kozai, S. Ikeda, M. Matsuka, T. Sakai, H. Matsumoto, *Electrochim. Acta* **2014**, *125*, 443.

[34] E. P. Antonova, A. S. Farlenkov, E. S. Tropin, V. A. Eremin, A. V. Khodimchuk, M. V. Ananyev, *Solid State Ionics* **2017**, *306*, 112.

[35] V. M. Goldschmidt, *Naturwissenschaften* **1926**, *14*, 477.

[36] R. D. Shannon, *Acta Cryst.* **1976**, *A32*, 751.

[37] N. Kochetova, I. Animitsa, D. Medvedev, A. Demin, P. Tsiakaras, *RSC Adv.* **2016**, *6*, 73222.

[38] E. Fabbri, A. D'Epifanio, E. Di Bartolomeo, S. Licoccia, E. Traversa, *Solid State Ionics* **2008**, *179*, 558.

[39] Y. Guo, Y. Lin, R. Ran, Z. Shao, *J. Power Sources* **2009**, *193*, 400.

[40] P. Sawant, S. Varma, B. N. Wani, S. R. Bharadwaj, *Int. J. Hydrogen Energy* **2012**, *37*, 3848.

[41] C. S. Tu, R. R. Chien, V. H. Schmidt, S. C. Lee, C. C. Huang, *J. Phys. Condens. Mater.* **2012**, *24*, 155403.

[42] L. Zhao, W. Tan, Q. Zhong, *Ionics* **2013**, *19*, 1745.

[43] N. Nasani, P. A. N. Dias, J. A. Saraiva, D. P. Fagg, *Int. J. Hydrogen Energy* **2013**, *38*, 8461.

[44] L. Lagaeva, D. Medvedev, A. Demin, P. Tsiakaras, *J. Power Sources* **2015**, *278*, 436.

[45] L. Malavasi, C. Tealdi, C. Ritter, V. Pomjakushin, F. Gozzo, Y. Diaz-Fernandez, *Chem. Mater.* **2011**, *23*, 1323.

[46] D. Han, M. Majima, T. Uda, *J. Solid State Chem.* **2013**, *205*, 122.

[47] C. Hiraiwa, D. Han, A. Kuramitsu, A. Kuwabara, H. Takeuchi, M. Majima, T. Uda, *J. Am. Ceram. Soc.* **2013**, *96*, 879.

[48] D. Han, K. Shinoda, T. Uda, *J. Am. Ceram. Soc.* **2014**, *97*, 643.

[49] A. K. E. Andersson, S. M. Selbach, C. S. Knee, T. Grande, *J. Am. Ceram. Soc.* **2014**, *97*, 2654.

[50] A. K. E. Andersson, S. M. Selbach, T. Grande, C. S. Knee, *Dalton Trans.* **2015**, *44*, 10834.

[51] V. Tsidilkovski, A. Kuzmin, L. Putilov, V. Balakireva, *Solid State Ionics* **2017**, *301*, 170.

[52] E. Jedvik, A. Lindman, M. Þ. Benediktsson, G. Wahnström, *Solid State Ionics* **2015**, *275*, 2.

[53] T. S. Bjørheim, A. Løken, R. Haugsrud, *J. Mater. Chem. A* **2016**, *4*, 5917.

[54] G. C. Mather, G. Heras-Juaristi, C. Ritter, R. O. Fuentes, A. L. Chinelatto, D. Pérez-Coll, U. Amador, *Chem. Mater.* **2016**, *28*, 4292.

[55] D. Han, N. Hatada, T. Uda, *J. Am. Ceram. Soc.* **2016**, *99*, 3745.

[56] R. Sažinas, M.-A. Einarsrud, T. Grande, *J. Mater. Chem. A* **2017**, *5*, 5846.

[57] S. R. Bishop, D. Marrocchelli, C. Chatzichristodoulou, N. H. Perry, M. B. Mogensen, H. L. Tuller, E. D. Wachsman, *Annu. Rev. Mater. Res.* **2014**, *44*, 205.

[58] R. Haugsrud, *Diff. Found.* **2016**, *8*, 31.

[59] K. H. Ryu, S. M. Haile, *Solid State Ionics* **1999**, *125*, 355.

[60] H. Matsumoto, Y. Kawasaki, N. Ito, M. Enoki, T. Ishihara, *Electrochem. Solid-State Lett.* **2007**, *10*, B77.

[61] D. Medvedev, A. Murashkina, E. Pikalova, A. Demin, A. Podias, P. Tsiakaras, *Prog. Mater. Sci.* **2014**, *60*, 72.

[62] L. Malavasi, C. A. J. Fisher, M. S. Islam, *Chem. Soc. Rev.* **2010**, *39*, 4370.

[63] Marrony M (ed.). *Proton-conducting Ceramics: From Fundamentals to Applied Research.* New York: Pan Stanford Publishing, **2016**.

[64] X. M. Liu, Z. G. Liu, J. H. Ouyang, Y. J. Gu, J. Xiang, F. Y. Yan, *Electrochim Acta* **2012**, *59*, 464.

[65] F. Zhao, Q. Liu, S. Wang, K. Brinkman, F. Chen , *Int. J. Hydrongen Energy* **2010**, *35*, 4258.

[66] X. Chi, J. Zhang, Z. Wen, Y. Liu, M. Wu, X. Wu, *J. Alloys Compd.* **2013**, *554*, 378.

[67] M. Zunic, G. Brankovic, C. R. Foschini, M. Cilense, E. Longo, J. A. Varela, *J. Alloys Compd.* **2013**, *563*, 254.

[68] X. M. Liu, Y. J. Gu, Z. G. Liu, J. H. Ouyang, F. Y. Yan, J. Xiang, *Bull. Mater. Sci.* **2013**, *36*, 395.

[69] A. Radojković, M. Žunić, S. M. Savić, G. Branković, Z. Branković, *Ceram. Int.* **2017**, *39*, 307.

[70] E. D. Bartolomeo, A. D'Epifanio, C. Pugnalini, F. Giannici, A. Longo, A. Martorana, S. Licoccia, *J. Power Sources* **2012**, *199*, 201.

[71] K. Xie, R. Yan, X. Chen, D. Dong, S. Wang, X. Liu, G. Meng, *J. Alloys Compd.* **2009**, *472*, 551.

[72] K. Xie, R. Yan, X. Xu, X. Liu, G. Meng, *Mater. Res. Bull.* **2009**, *44*, 1474.

[73] K. Xie, R. Yan, X. Xu, X. Liu, G. Meng, *J. Power Sources* **2009**, *187*, 403.

[74] K. Xie, R. Yan, X. Chen, S. Wang, Y. Jiang, X. Liu, G. Meng, *J. Alloys Compd.* **2009**, *473*, 323.

[75] R. Yan, Q. Wang, K. Xie, *Ionics* **2009**, *15*, 501.

[76] A. Lindman, E. E. Helgee, G. Wahnström, *Chem. Mater.* **2017**, *29*, 7931.

[77] A. Bassano, V. Buscaglia, M. Viviani, M. Bassoli, M. T. Buscaglia, M. Sennour, A. Thorel, P. Nanni, *Solid State Ionics* **2009**, *180*, 168.

[78] M. Shirpour, R. Merkle, C. T. Lin, J. Maier, *Phys. Chem. Chem. Phys.* **2012**, *14*, 730.

[79] S. Wienströer, H.-D. Wiemhöfer, *Solid State Ionics* **1997**, *101-103*, 1113.

[80] K. H. Ryu, S. M. Haile, *Solid State Ionics* **1999**, *125*, 355.

[81] Z. Shao, W. Zhou, Z. Zhu, *Prog. Mater. Sci.* **2012**, *57*, 804.

[82] Y.-G. Guo, J.-S. Hu, L.-J. Wan, *Adv. Mater.* **2008**, *20*, 2878.

[83] J. H. Shim, *Nat. Energy* **2018**, *3*, 168.

[84] B. S. Prakash, R. Pavitra, S. S. Kumar, S. T. Aruna, *J. Power Sources* **2018**, *381*, 136.

[85] Y. H. Lee, I. Chang, G. Y. Cho, J. Park, W. Yu, W. H. Tanveer, S. W. Cha, *Int. J. Precis. Eng. Manuf.* **2018**, *5*, 441.

[86] A. Volkov, E. Gorbova, A. Vylkov, D. Medvedev, A. Demin, P. Tsiakaras, *Sens. Actuators B* **2017**, *244*, 1004.

[87] D. A. Medvedev, A. A. Murashkina, A. K. Demin, *Rev. J. Chem.* **2015**, *5*, 193.

[88] L. Bi, E. Traversa, *J. Mater. Res.* **2014**, *29*, 1.

[89] D. Hassan, S. Janes, R. Clasen, *J. Eur. Ceram. Soc.* **2003**, *23*, 221.

[90] S. Yamanaka, M. Fujikane, T. Hamaguchi, H. Muta, T. Oyama, T. Matsuda, S.-I. Kobayashi, K. Kurosaki, *J. Alloys Compd.* **2003**, *359*, 109.

[91] P.-F. Yang, D.-L. Chen, S.-R. Jian, S.-W. Lee, C.-J. Tseng, *Proced. Eng.* **2014**, *79*, 599.

[92] E. V. Tsipis, V. V. Kharton, *J. Solid State Electrochem.* **2008**, *12*, 1039.

[93] J. Lyagaeva, B. Antonov, L. Dunyushkina, V. Kuimov, D. Medvedev, A. Demin, P. Tsiakaras, *Electrochim. Acta* **2016**, *192*, 80.

[94] K. Xie, R. Yan, X. Xu, X. Liu, G. Meng, *J. Power Sources* **2009**, *187*, 403.

[95] E. Gorbova, V. Maragou, D. Medvedev, A. Demin, P. Tsiakaras, *J. Power Sources* **2008**, *181*, 207.

[96] Q. Nian, L. Zhao, B. He, B. Lin, R. Peng, G. Meng, X. Liu, *J. Alloys Compd.* **2010**, *492*, 291.

[97] Z. Zhu, Z. Tao, L. Bi, W. Liu, *Mater. Res. Bull.* **2010**, *45*, 1771.

[98] Yu. G. Lyagaeva, D. A. Medvedev, A. K. Demin, P. Tsiakaras, O. G. Reznitskikh, *Phys. Solid State* **2015**, *57*, 285.

[99] L. Yang, Z. Liu, S. Wang, Y. M. Choi, C. Zuo, M. Liu, *J. Power Sources* **2010**, *195*, 471.

[100] Y. Chen, Q. Gu, D. Tian, Y. Ding, X. Lu, W. Yu, T. T. Isimjan, B. Lin, *Int. J. Hydrogen Energy* **2014**, *39*, 13665.

[101] Z. Zhu, J. Qian, Z. Wang, J. Dang, W. Liu, *J. Alloys Compd.* **2013**, *581*, 832.

[102] X. Zhou, L. Liu, J. Zhen, S. Zhu, B. Li, K. Sun, P. Wang, *J. Power Sources* **2011**, *196*, 5000.

[103] S. Wang, F. Zhao, L. Zhang, F. Chen, *Solid State Ionics* **2012**, *213*, 29.

[104] R. A. De Souza, Z. A. Munir, S. Kim, M. Martin, *Solid State Ionics* **2011**, *196*, 1.

[105] B. Madhavan, A. Ashok, *Ionics* **2015**, *21*, 601.

[106] S. Nikodemski, J. Tong, C. Duan, R. O'Hayre, *Solid State Ionics* **2016**, *294*, 37.

[107] S. Nikodemski, J. Tong, R. O'Hayre, *Solid State Ionics* **2013**, *253*, 201.

[108] H.-I. Ji, B.-K. Kim, J. H.Yu, S.-M. Choi, H.-R. Kim, J.-W. Son, H.-W. Lee, J.-H. Lee, *Solid State Ionics* **2011**, *203*, 9.

[109] G. Heras-Juaristi, D. Pérez-Coll, G. C. Mather, *J. Power Sources* **2017**, *364*, 52.

[110] N. A. Danilov, J. G. Lyagaeva, D. A. Medvedev, A. K. Demin, P. Tsiakaras, *Electrochim. Acta* **2018**, *284*, 551.

[111] E. Gilardi, E. Fabbri, L. Bi, J. L. M. Rupp, T. Lippert, D. Pergolesi, E. Traversa, *J. Phys. Chem. C* **2017**, *121*, 9739.

[112] N. Danilov, E. Pikalova, J. Lyagaeva, B. Antonov, D. Medvedev, A. Demin, P. Tsiakaras, *J. Power Sources*, **2017**, *366*, 161.

[113] J. Lyagaeva, G. Vdovin, L. Hakimova, D. Medvedev, A. Demin, P. Tsiakarasa, *Electrochim. Acta* **2017**, *251*, 554.

[114] D. Han, N. Hatada, T. Uda, *J. Electrochem. Soc.* **2016**, *163*, F470.

[115] D. Han, K. Shinoda, S. Sato, M. Majima, T. Uda, *J. Mater. Chem. A* **2015**, *3*, 1243.

[116] T. Yajima, H. Iwahara, H. Uchida, *Solid State Ionics* **1991**, *47*, 117.

[117] C. Zhang, H. Zhao, *Solid State Ionics* **2010**, *181*, 1478.

[118] S. Wang, F. Zhao, L. Zhang, K. Brinkman, F. Chen, *J. Alloys Compd.* **2010**, *506*, 263.

[119] J. Madhuri Sailaja, N. Murali, K. Vijay Babu, V. Veeraiah, *J. Asian Ceram. Soc.* **2017**, *5*, 18.

[120] N. Radenahmad, A. Afif, M. I. Petra, S. M. H. Rahman, S. Eriksson, A. K. Azad, *Int. J. Hydrogen Energy* **2016**, *41*, 11832.

[121] K. Singh, A. K. Baral, V. Thangadurai, *J. Am. Ceram. Soc.* **2016**, *99*, 866.

[122] K. Singh, R. Kannan, V. Thangadurai, *Int. J. Hydrogen Energy* **2016**, *41*, 13227.

[123] J. M. Sailaja, K. V. Babu, N. Murali, V. Veeraiah, *J. Adv. Res.* **2017**, *8*, 169.

[124] K.-R. Lee, C.-J. Tseng, J.-K. Chang, K.-W. Wang, Y.-S. Huang, T.-C. Chou, K.-C. Chiu, L.-D. Tsai, S.-W. Lee, *Int. J. Hydrogen Energy* **2017**, *42*, 22222.

[125] T. Amiri, K. Singh, N. K. Sandhu, A. R. Hanifi, T. H. Etsell, J.-L. Luo, V. Thangadurai, P. Sarkar, *J. Electrochem. Soc.* **2018**, *165*, F764.

[126] Y. Zhang, R. Knibbe, J. Sunarso, Y. Zhong, W. Zhou, Z. Shao, Z. Zhu, *Adv. Mater.* **2017**, *29*, 1700132.

[127] C. Duan, D. Hook, Y. Chen, J. Tong, R. O'Hayre, *Energy Environ. Sci.* **2017**, *10*, 176.

[128] R. Strandbakke, V. A.Cherepanov, A. Y. Zuev, D. S. Tsvetkov, C. Argirusis, G. Sourkouni, S. Prünte, T. Norby, *Solid State Ionics* **2015**, *278*, 120.

[129] S. Sun, Z. Cheng, *J. Electrochem. Soc.* **2017**, *164*, F3104.

[130] B. Hu, C. Xia, *Asia-Pac. J. Chem. Eng.* **2016**, *11*, 327.

[131] J. T. S. Irvine, D. Neagu, M. C. Verbraeken, C. Chatzichristodoulou, C. Graves, M. B. Mogensen, *Nature Energy* **2016**, *1*, 15014.

[132] W. H. Kan, A. J. Samson, V. Thangadurai, *J. Mater. Chem. A* **2016**, *4*, 17913.

[133] Y. Li, W. Zhang, Y. Zheng, J. Chen, B. Yu, Y. Chen, M. Liu, *Chem. Soc. Rev.* **2017**, *46*, 6345.

[134] D. Lee, H. N. Lee, *Materials* **2017**, *10*, 368.

[135] N. H. Perry, T. Ishihara, *Materials* **2016**, *9*, 858.

[136] A. Grimaud, F. Mauvy, J. M. Bassat, S. Fourcade, L. Rocheron, M. Marrony, J. C. Grenier, *J. Electrochem. Soc.* **2012**, *159*, B683.

[137] F. He, T. Wu, R. Peng, C. Xia, *J. Power Sources* **2009**, *194*, 263.

[138] C.-Y. Yoo, D. S. Yun, S.-Y. Park, J. Park, J. H. Joo, H. Park, M. Kwak, J. H. Yu, *Electrocatal.* **2016**, *7*, 280.

[139] A. Grimaud, J.-M. Bassat, F. Mauvy, M. Pollet, A. Wattiaux, M. Marrony, J.-C. Grenier, *J. Mater. Chem. A* **2014**, *2*, 3594.

[140] R. Zohourian, R. Merkle, G. Raimondi, J. Maier, *Adv. Funct. Mater.* **2018**, DOI: 10.1002/adfm.201801241.

[141] J. Kim, S. Sengodan, G. Kwon, D. Ding, J. Shin, M. Liu, G. Kim, *ChemSusChem* **2014**, *7*, 2811.

[142] C. Duan, J. Tong, M. Shang, S. Nikodemski, M. Sanders, S. Ricote, A. Almansoori, R. O'Hayre, *Science* **2015**, *349*, 1321.

[143] H. T. Lozano, J. Druce, S. J. Cooper, J.A. Kilner, *Sci. Technol. Adv. Mater.* **2017**, *18*, 977.

[144] S. Sun, Z. Cheng, *J. Electrochem. Soc.* **2017**, *164*, F81.

[145] A. Grimaud, F. Mauvy, J. M. Bassat, S. Fourcade, M. Marrony, J. C. Grenier, *J. Mater. Chem.* **2012**, *22*, 16017.

[146] J. Cheng, S. Zhang, B. Meng, J. Ding, X. Tan, *J. Alloys Compd.* **2018**, *742*, 966.

[147] J. Xue, Q. Liao, W. Chen, H. J. M. Bouwmeester, H. Wang, A. Feldhoff, *J. Mater. Chem. A* **2015**, *3*, 19107.

[148] E. Yu. Pikalova, D. A. Medvedev, A. F. Khasanov, *Phys. Solid State* **2017**, *59*, 694.

[149] J. Lyagaeva, D. Medvedev, E. Pikalova, S. Plaksin, A. Brouzgou, A. Demin, P. Tsiakaras, *Int. J. Hydrogen Energy* **2017**, *42*, 1715.

[150] V. V. Kharton, A. V. Kovalevsky, M. Avdeev, E. V. Tsipis, M. V. Patrakeev, A. A. Yaremchenko, E. N. Naumovich, J. R. Frade, *Chem. Mater.* **2007**, *19*, 2027.

[151] Yu. G. Lyagaeva, N. A. Danilov, M. Yu. Gorshkov, G. K. Vdovin, B. D. Antonov, A. K. Demin, D. A. Medvedev, *Russ. J. Appl. Chem.* **2018**, *91*, 583.

[152] E. Kravchenko, K. Zakharchuk, A. Viskup, J. Grins, G. Svensson, V. Pankov, A. Yaremchenko, *ChemSusChem* **2017**, *10*, 600.

[153] V. A. Sadykov, E. Yu. Pikalova, A. A. Kolchugin, E. A. Filonova, E. M. Sadovskaya, N. F. Eremeev, A. V. Ishchenko, A. V. Fetisov, S. M. Pikalov, *Solid State Ionics* **2018**, *317*, 234.

[154] N. M. Porotnikova, A. V. Khodimchuk, M. V. Ananyev, V. A. Eremin, E. S. Tropin, A. S. Farlenkov, E. Yu. Pikalova, A. V. Fetisov, *J. Solid State Electrochem.* **2018**, *22*, 2115.

[155] V. A. Sadykov, E. M. Sadovskaya, E. Yu. Pikalova, A. A. Kolchugin, E. A. Filonova, S. M. Pikalov, N. F. Eremeev, A. V. Ishchenko, A. I. Lukashevich, J. M. Bassat, *Ionics* **2018**, *24*, 1181.

[156] A. Zhu, G. Zhang, T. Wan, T. Shi, H Wang, M. Wu, C. Wang, S. Huang, Y. Guo, H. Yu, Z. Shao, *Electrochim. Acta* **2018**, *259*, 559.

[157] L. Zhao, B. He, Y. ling, Z. Xun, R. Peng, G. Meng, X. Liu, *Int. J. Hydrogen Energy* **2010**, *35*, 3769.

[158] E. P. Antonova, A. A. Kolchugin, E. Yu. Pikalova, D. A. Medvedev, N. M. Bogdanovich, *Solid State Ionics* **2017**, *306*, 55.

[159] X.-M. Ge, S.-H. Chan, Q.-L. Liu, Q. Sun, *Adv. Energy Mater.* **2012**, *2*, 1156.

[160] W. Wang, C. Su, Y. Wu, R. Ran, Z. Shao, *Chem. Rev.* **2013**, *113*, 8104.

[161] A. Faes, A. Hessler-Wyser, A. Zryd, J. Van herle, *Membranes* **2012**, *2*, 585.

[162] W. H. Kan, V. Thangadurai, *Ionics* **2015**, *21*, 301.

[163] Y.-E. Park, H.-I. Ji, B.-K. Kim, J.-H. Lee, H.-W. Lee, J.-S. Park, *Ceram. Int.* **2013**, *39*, 2581.

[164] P. Sawant, S. Varma, M. R. Gonal, B. N. Wani, D. Prakash, S. R. Bharadwaj, *Electrochim. Acta* **2014**, *120*, 80.

[165] B. H. Rainwater, M. Liu, M. Liu, *Int. J. Hydrogen Energy* **2012**, *37*, 18342.

[166] M. Zunic, G. Brankovic, C. R. Foschini, M. Cilense, E. Longo, J. A. Varela, *J. Alloys Compd.* **2013**, *563*, 254.

[167] M. Li, B. Hua, J.-L. Luo, S. P. Jiang, J. Pu, B. Chi, L. Jian, *J. Mater. Chem. A* **2015**, *3*, 21609.

[168] W. G. Coors, A. Manerbino, *J. Membr. Sci.* **2011**, *376*, 50.

[169] N. Narendar, G. C. Mather, P. A. N. Dias, D. P. Fagg, *RSC Adv.* **2013**, *3*, 859.

[170] N. Nasani, D. Ramasamy, A. D. Brandão, A. A. Yaremchenko, D. P. Fagg, *Int. J. Hydrogen Energy* **2014**, *39*, 21231.

[171] K. Miyazaki, T. Okanishi, H. Muroyama, T. Matsui, K. Eguchi, *J. Power Sources* **2017**, *365*, 148.

[172] H. Ding, N. P. Sullivan, S. Ricote, *Solid State Ionics* **2017**, *306*, 97.

[173] T. G. Howell, C. P. Kuhnell, T. L. Reitz, A. M. Sukeshini, R. N. Singh, *J. Power Sources* **2013**, *231*, 279.

[174] C. Graves, B. R. Sudireddy, M. Mogensen, *ECS Trans.* **2010**, *28*, 173.

[175] L. S. Skutina, A. I. Vylkov, D. A. Medvedev, E. A. Filonova, *J. Alloys Compd.* **2017**, *705*, 854.

[176] L. Zhang, Q. Zhou, Q. He, T. He, *J. Power Sources* **2010**, *195*, 6356.

[177] A. B. Muñoz-García, M. Pavone, *J. Mater. Chem. A* **2017**, *5*, 12735.

[178] A. B. Muñoz-García, M. Pavone, *Int. J. Quantum Chem.* **2016**, *116*, 1501.

[179] T. Norby, *Solid State Ionics* **1988**, *28-30*, 1586.

[180] D. P. Sutija, T. Norby, P. Björnbom, *Solid State Ionics* **1995**, *77*, 167.

[181] A. Demin, P. Tsiakaras, *Int. J. Hydrogen Energy* **2001**, *26*, 1103.

[182] T. Nakamura, S. Mizunuma, Y. Kimura, Y. Mikami, K. Yamauchi, T. Kuroha, N. Taniguchi, Y. Tsuji, Y. Okuyama, K. Amezawa, *J. Mater. Chem. A* **2018**, *6*, 15771.

[183] H.-I. Ji, H. Kim, H.-W. Lee, B.-K. Kim, J.-W. Son, K.J. Yoon, J.-H. Lee, *Phys. Chem. Chem. Phys.* **2018**, *20*, 14997.

[184] H. Taherparvar, J. A. Kilner, R. T. Baker, M. Sahibzada, *Solid State Ionics* **2003**, *162-163*, 297.

[185] F. He, D. Song, R. Peng, G. Meng, S. Yang, *J. Power Sources* **2010**, *195*, 3359.

[186] D.-K. Lim, H.-N. Im, B. Singh, S.-J. Song, *J. Electrochem. Soc.* **2015**, *162*, F547.

[187] K.-C. Lee, M.-B. Choi, D.-K. Lim, B. Singh, S.-J. Song, *J. Power Sources* **2013**, *232*, 224.

[188] D.-K. Lim, J.-H. Kim, A. U. Chavan, T.-R. Lee, Y.-S. Yoo, S.-J. Song, *Ceram. Int.* **2016**, *42*, 3776.

[189] E. Pikalova, D. Medvedev, *Int. J. Hydrogen Energy* **2016**, *41*, 4016.

[190] N. Shi, F. Su, D. Huan, Y. Xie, J. Lin, W. Tan, R. Peng, C. Xia, C. Chen, Y. Lu, *J. Mater. Chem. A* **2017**, *5*, 19664.

[191] N. Danilov, J. Lyagaeva, G. Vdovin, D. Medvedev, A. Demin, P. Tsiakaras, *ACS Appl. Mater. Interfaces* **2017**, *9*, 26874.

[192] M. A. Azimova, S. McIntosh, *Solid State Ionics* **2011**, *203*, 57.

[193] S. M. Babiniec, S. Ricote, N. P. Sullivan, *Int. J. Hydrogen Energy* **2015**, *40*, 9278.

[194] N. Danilov, J. Lyagaeva, G. Vdovin, E. Pikalova, D. Medvedev, *Energy Convers. Manag.* **2018**, *172*, 129.

[195] H. Zhu, S. Ricote, C. Duan, R. O'Hayre, D. S. Tsvetkov, R. J. Kee, *J. Electrochem. Soc.* **2018**, *165*, F581.

[196] H. Zhu, S. Ricote, C. Duan, R. O'Hayre, R. J. Kee, *J. Electrochem. Soc.* **2018**, *165*, F845.

[197] K. Chen, S. P. Jiang, *J. Electrochem. Soc.* **2016**, *163*, F3070.

[198] A. Lanzini, H. Madi, V. Chiodo, D. Papurello, S. Maisano, M. Santarelli, J. Van herle, *Prog. Energy Combust. Sci.* **2017**, *61*, 150.

[199] M. Martin, *J. Korean Ceram. Soc.* **2012**, *49*, 29.

[200] C. Zhang, J. Sunarso, S. Liu, *Chem. Soc. Rev.* **2017**, *46*, 2941.

[201] D. K. Niakolas, *Appl. Catal. A: Gen.* **2014**, *486*, 123.

[202] S. Yang, Y. Wen, S. Zhang, S. Gu, Z. Wen, X. Ye, *Int. J. Hydrogen Energy* **2017**, *42*, 28549.

[203] H. Li, X. Chen, S. Chen, Y. Wu, K. Xie, *Int. J. Hydrogen Energy* **2015**, *40*, 7920.

[204] X.-F. Ye, Y. B. Wen, S. J. Yang, Y. Lu, W. H. Luo, Z. Y. Wen, J. B. Meng, *Int. J. Hydrogen Energy* **2017**, *42*, 23189.

[205] L. Bi, E. Traversa, *ECS Trans.* **2015**, *68*, 3387.

[206] S. Choi, C. J. Kucharczyk, Y. Liang, X. Zhang, I. Takeuchi, H.-I. Ji, S.M. Haile, *Nat. Energy* **2018**, *3*, 202.

[207] H. Shi, Z. Ding, G. Ma, *Fuel Cells* **2016**, *16*, 258.

[208] X. Mao, W. Wang, G. Ma, *Ceram. Int.* **2015**, *41*, 10276.

[209] J. Lyagaeva, N. Danilov, A. Tarutin, G. Vdovin, D. Medvedev, A. Demin, P. Tsiakaras, *Dalton Trans.* **2018**, *47*, 8149.

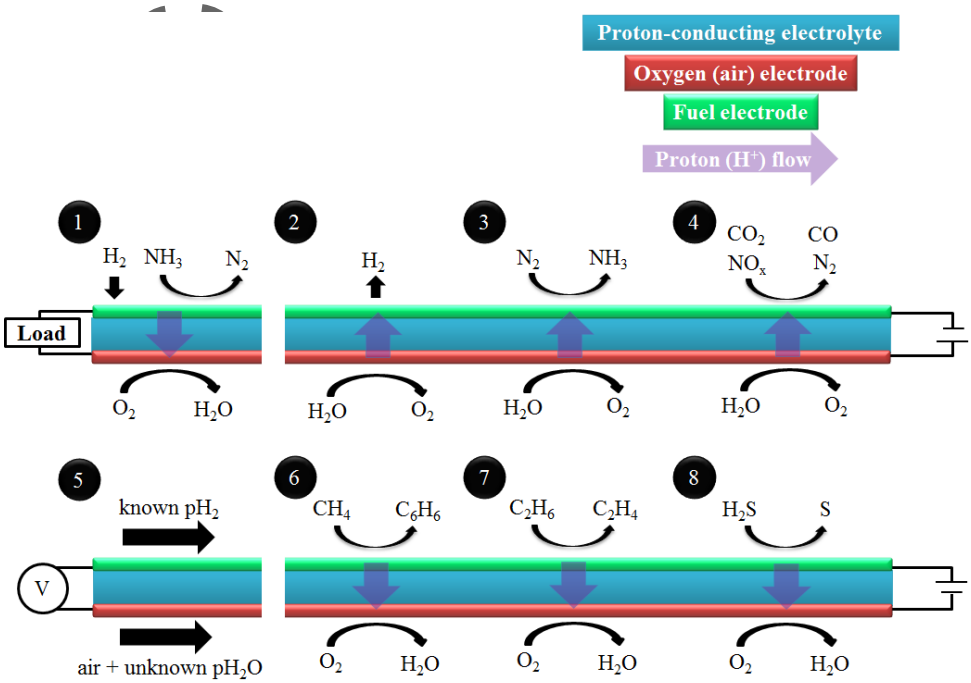

Figure 1. The main types of SOCs based on proton-conducting materials: 1 – H_2- or NH_3-fueled fuel cells, 2 – electrolysis cells, 3 – ammonia synthesis reactors, 4 – reactors of CO_2 or NO_x reduction, 5 – potentiometric-type sensors and reactors of compounds dehydrogenation with the formation of aromatics (6), alkenes (7) and sulfur (8).

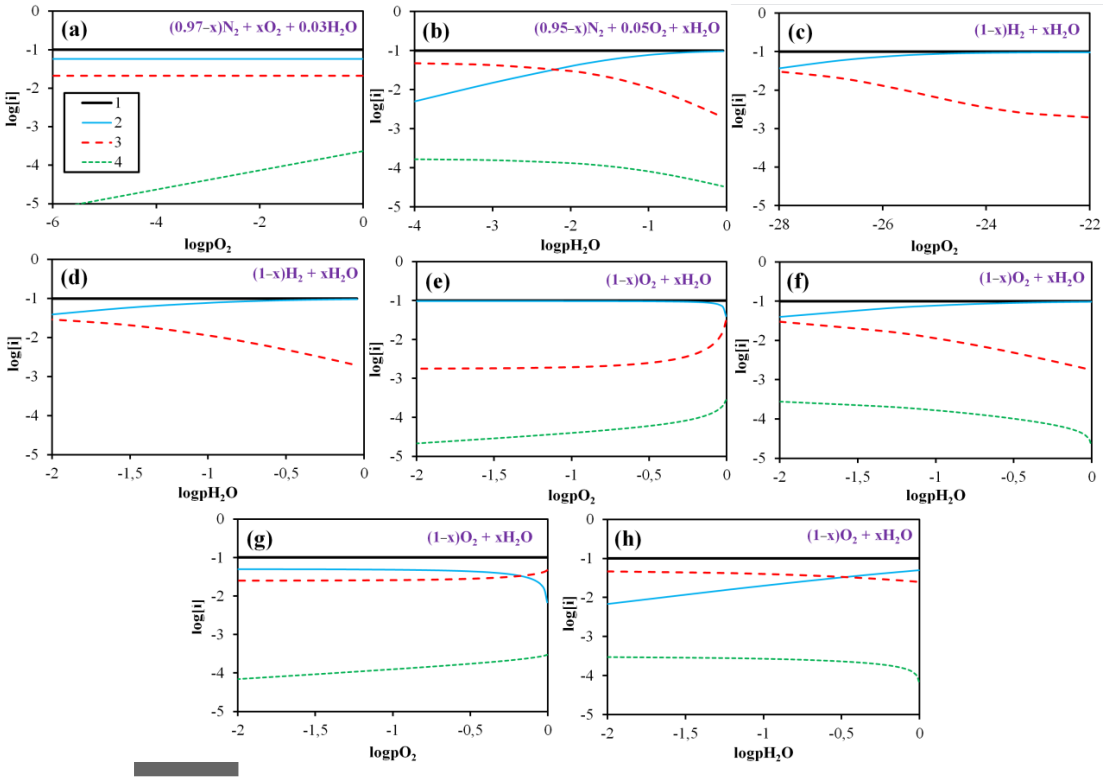

Figure 2. Concentration dependences of the mobile defects on the pO_2 and pH_2O variation in different model atmospheres: 1 – $[M_B^{/}]$, 2 – $[OH_O^{\bullet\bullet}]$, 3 – $[V_O^{\bullet\bullet}]$ and 4 – $[h^{\bullet}]$. The concentrations are presented in relative units, dopant concentration ($[M_B^{/}]$) is equal to 0.1. The parameters K_w and K_p are set as 5.3 and 2.6×10^{-6} (a low temperature, a-f) and 0.1 and 1.9×10^{-6} (a high temperature, g and h).

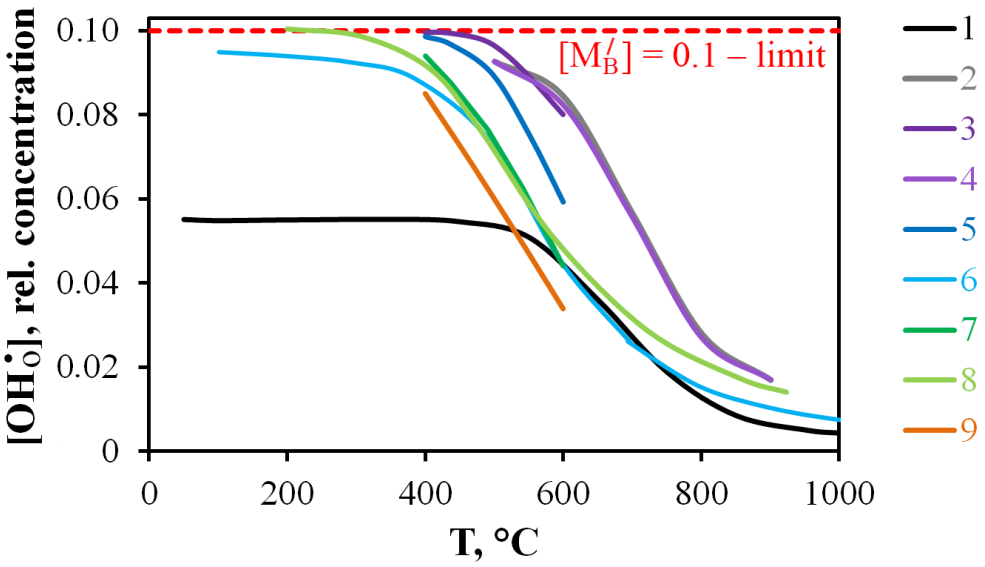

Figure 3. Proton concentration and hydration behavior of perovskite materials based on barium cerate and barium zirconate as a function of temperature. The correlation of the numbers, materials and references can be found in Table 1. The concentration of acceptor dopants is kept at 0.1. The curves were obtained at moderately moist conditions with a pH_2O of around 0.02 atm.

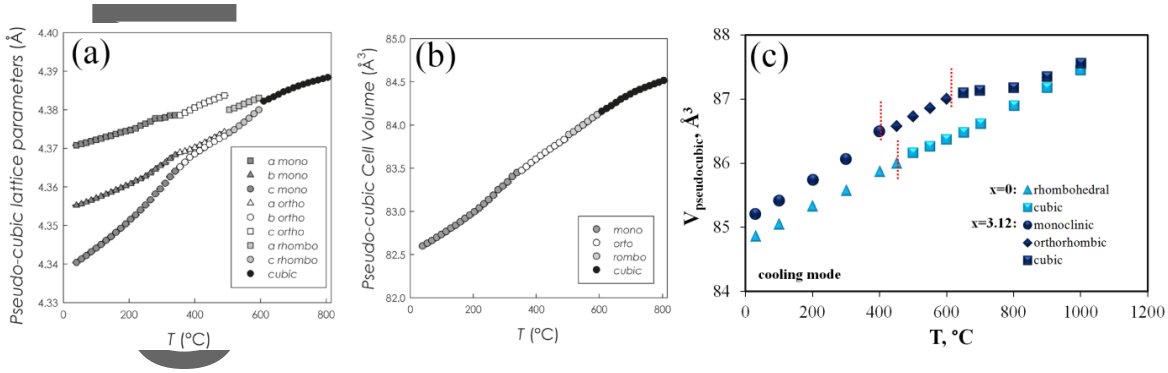

Figure 4. The temperature dependences of unit cell parameters (a) and lattice volume (b) of the $BaCe_{0.65}Zr_{0.2}Y_{0.15}O_{3-\delta}$ sample in static air. (a,b) Reproduced with permission.[45] Copyright 2011, American Chemical Society. (c) The temperature dependences of preudocubic cell volume of the $BaCe_{0.8}Y_{0.2}O_{3-\delta}$ sample in oxygen atmospheres with different humidity, O_2 + x vol.% H_2O. Reproduced with permission.[46] Copyright 2013, Elsevier.

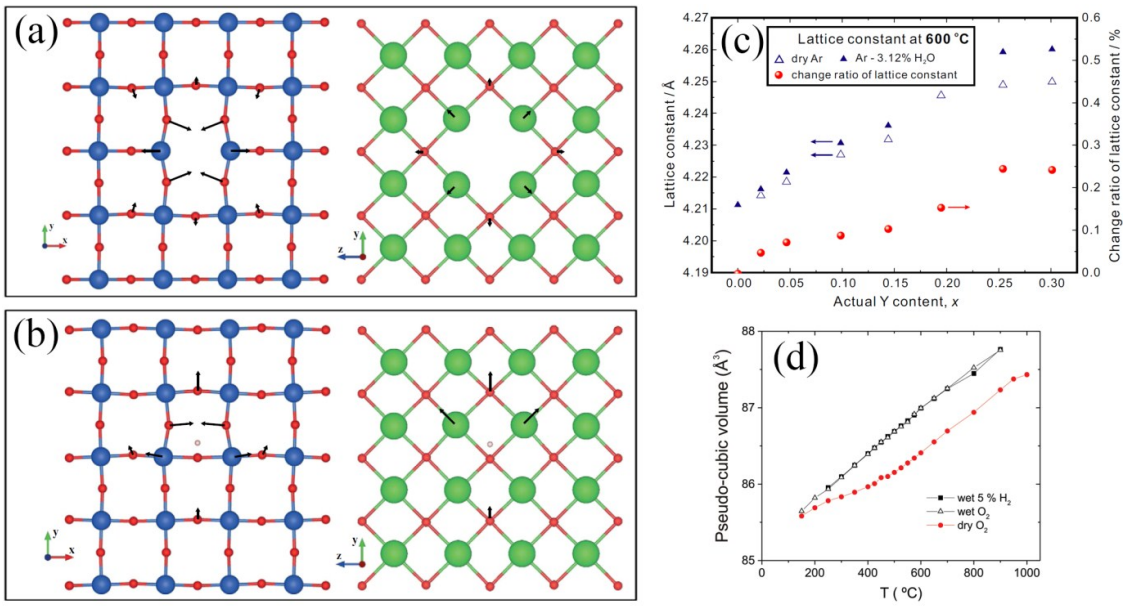

Figure 5. The lattice distortions of Zr- and Ba-sublattices in the presence of oxygen vacancies (a) and protons (b). (a,b) Reproduced with permission.[52] Copyright 2015, Elsevier. (c) Lattice constant of $BaZr_{1-x}Y_xO_{3-\delta}$ obtained in different atmospheres. The data are obtained from the X-ray diffraction under cooling mode. Reproduced with permission.[51] Copyright 2016, WILEY-VCH Verlag GmbH & Co. KGaA, Weinheim. (d) The pseudo-cubic cell volume of $BaCe_{0.8}Y_{0.2}O_{3-\delta}$ in different atmospheres. The data are obtained from the neutron diffraction analysis under cooling mode. Reproduced with permission.[50] Copyright 2015, Royal Society of Chemistry.

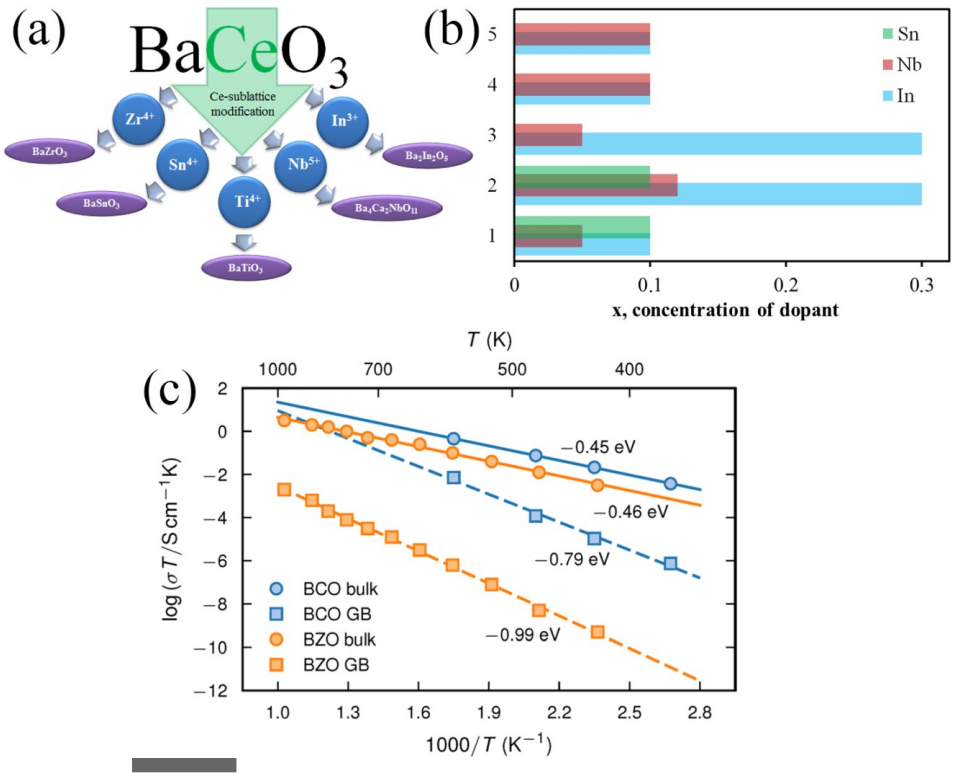

Figure 6. (a) Possible modification ways of $BaCeO_3$ to enhance its chemical stability as well as the representative of proton-conducting oxides with complete substitution of Ce^{4+} cations by the dopants. (b) The concentration of stabilizing dopant in $BaCeO_3$ to obtain enhanced chemical stability in H_2O- and/or CO_2-containing atmospheres; In-doped system: 1 – [64], 2 – [65], 3 – [66], 4 – [67], 5 – [68]; Nb-doped system: 1 – [69], 2 – [70], 3 – [71], 4 – [72], 5 – [73]; Sn-doped system: 1 – [74], 2 – [75]. (c) bulk and grain boundary conductivity of doped $BaCeO_3$ and $BaZrO_3$ materials. The graph is presented in literature[76] based on the published data in literature[77,78]. Reproduced with permission.[76] Copyright 2017, American Chemical Society.

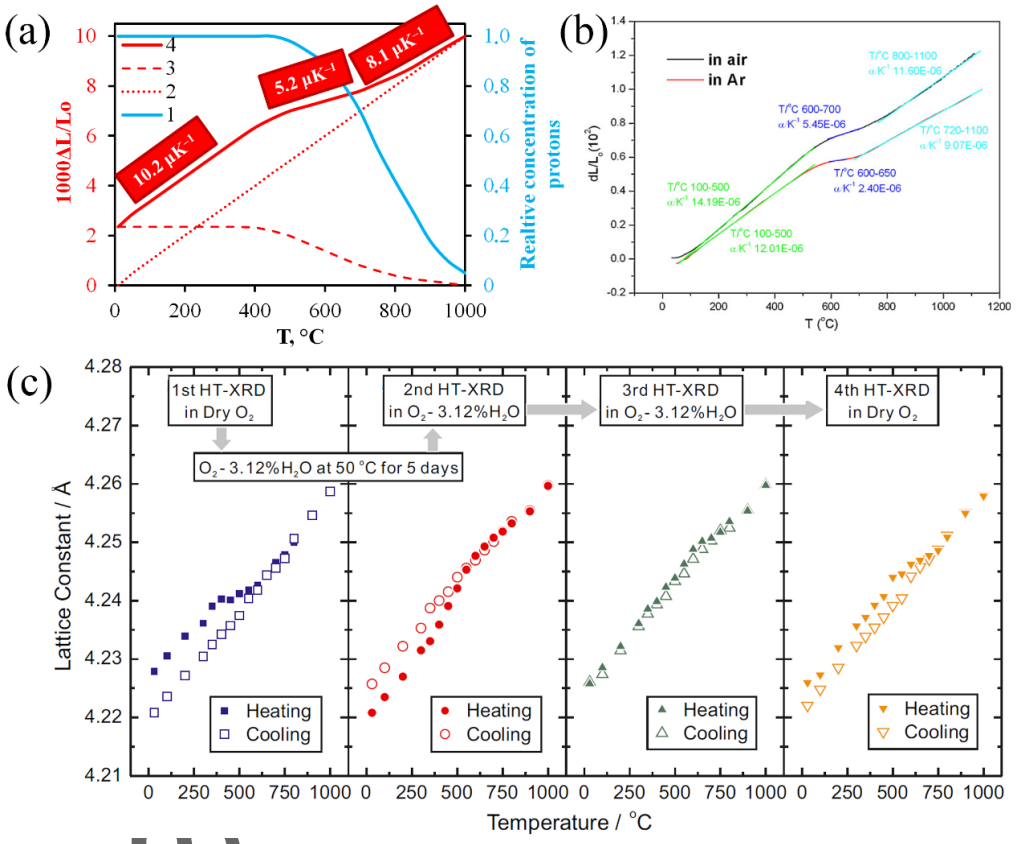

Figure 7. (a) Chemical and thermal expansion profiles of a dried (dehydrated) proton conductor under cooling in water-containing atmosphere and calculated TEC values from the temperature dependence of measured expansion: 1 – ratio of real concentration of protons to the maximal one, 2 – thermal expansion, 3 – chemical expansion, 4 – measured expansion. (b) Thermal expansion curves of the $BaCe_{0.7}Zr_{0.1}Y_{0.1}Yb_{0.1}O_{3-\delta}$ (BCZYYb) sample measured in various atmospheres. Reproduced with permission.[102] Copyright 2011, Elsevier. (c) Lattice constant change in a $BaZr_{0.8}Y_{0.2}O_{3-\delta}$ pellet sample with various temperatures, obtained by continuous high-temperature (HT)-XRD measurements in different atmospheres. Reproduced with permission.[47] Copyright 2013, WILEY-VCH Verlag GmbH & Co. KGaA, Weinheim.

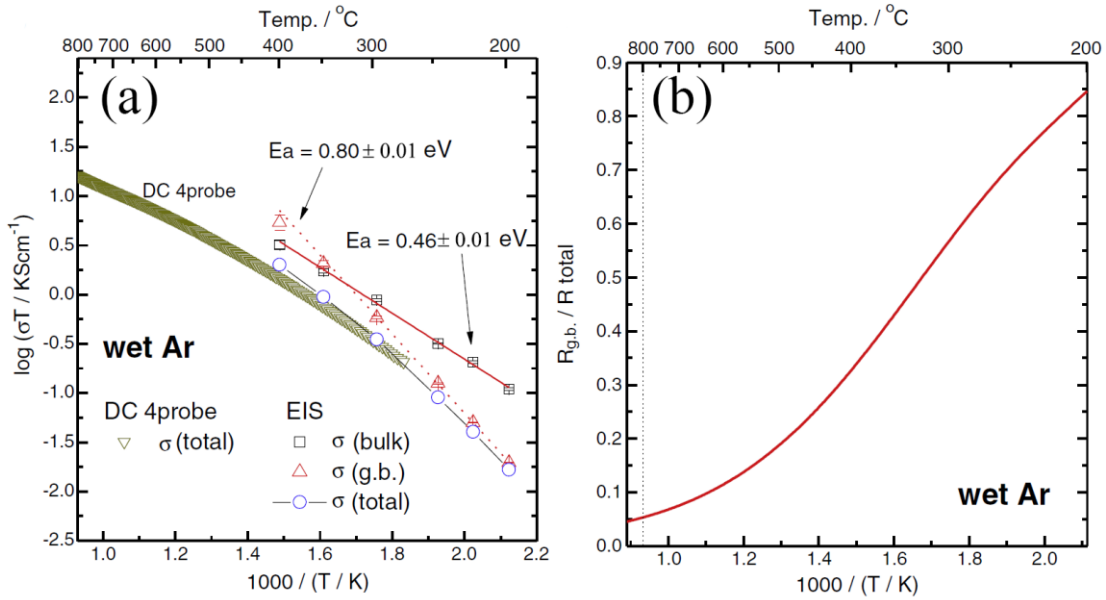

Figure 8. The comparison of total conductivities of $BaZr_{0.85}Y_{0.15}O_{3-\delta}$ measured by EIS and DC methods in wet Ar condition (a), and the ratio of grain boundary resistance to total resistance with respect to temperature (b). (a,b) Reproduced with permission.[108] Copyright 2011, Elsevier.

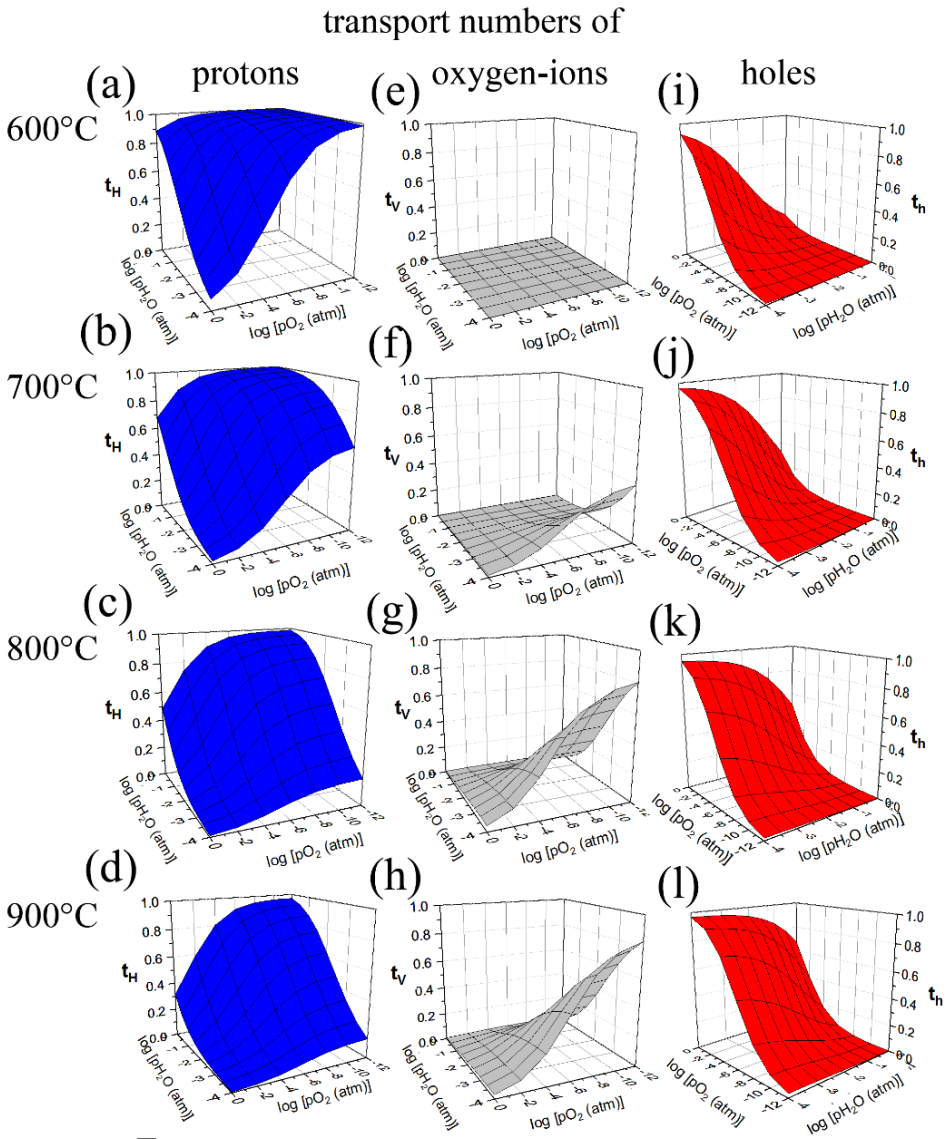

Figure 9. Protonic (a–d), oxygen-ionic (e–h) and electron-hole (i–l) transport numbers as functions of pO_2 and pH_2O at different temperatures. All panels reproduced with permission.[109] Copyright 2017, Elsevier.

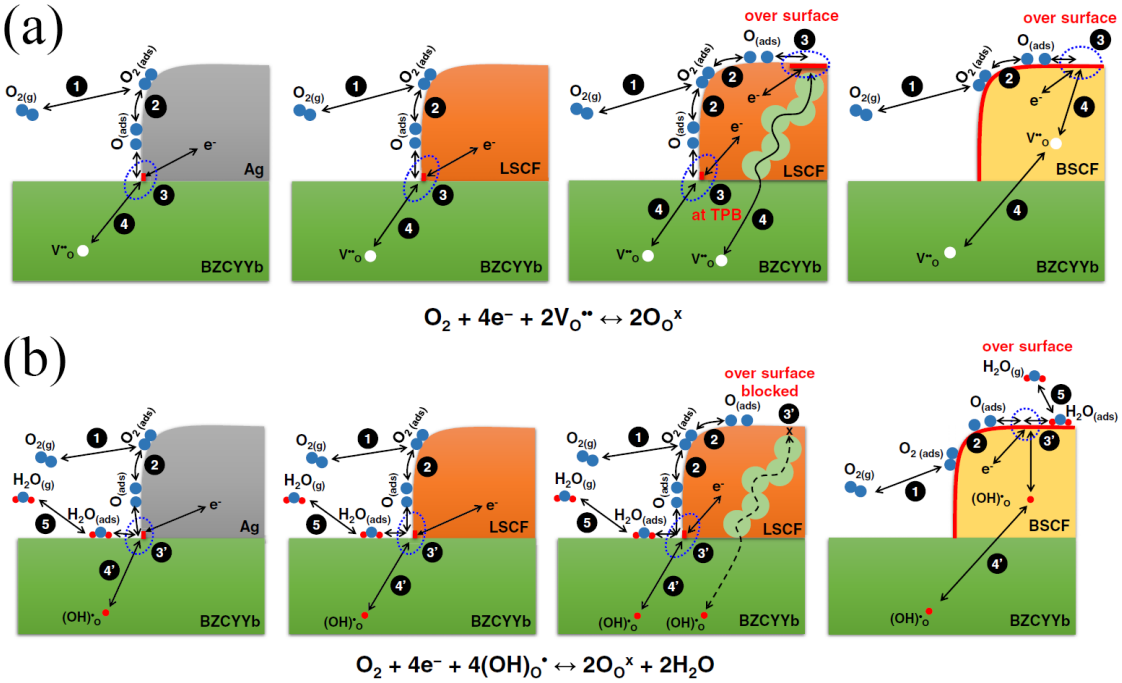

Figure 10. Schematic representation of possible reactions for SOFCs based on different electrodes and pure oxygen-ionic (a) and proton-conducting (b) electrolytes. All panels reproduced with permission.[129] Copyright 2017, The Electrochemical Society.

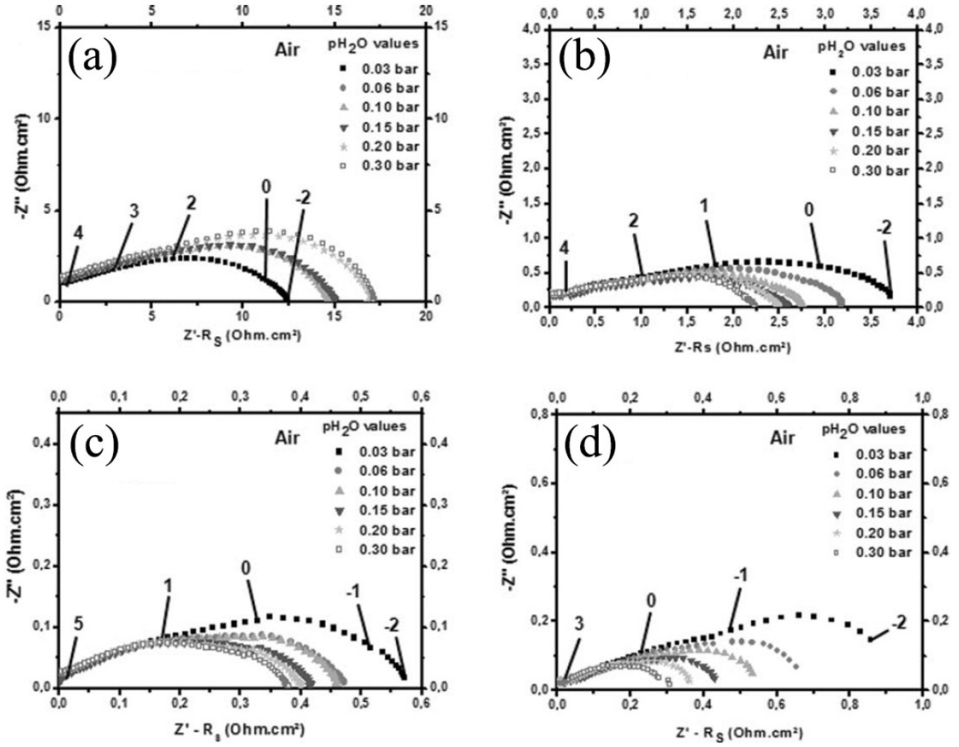

Figure 11. Impedance spectra recorded at 600 °C, under air atmospheres containing 0.03 to 0.30 bar of steam for the symmetrical cells with the following oxygen electrodes: LSFC (a), BSCF (b), PBC (c) and PN (d). All panels reproduced with permission.[136] Copyright 2012, The Electrochemical Society.

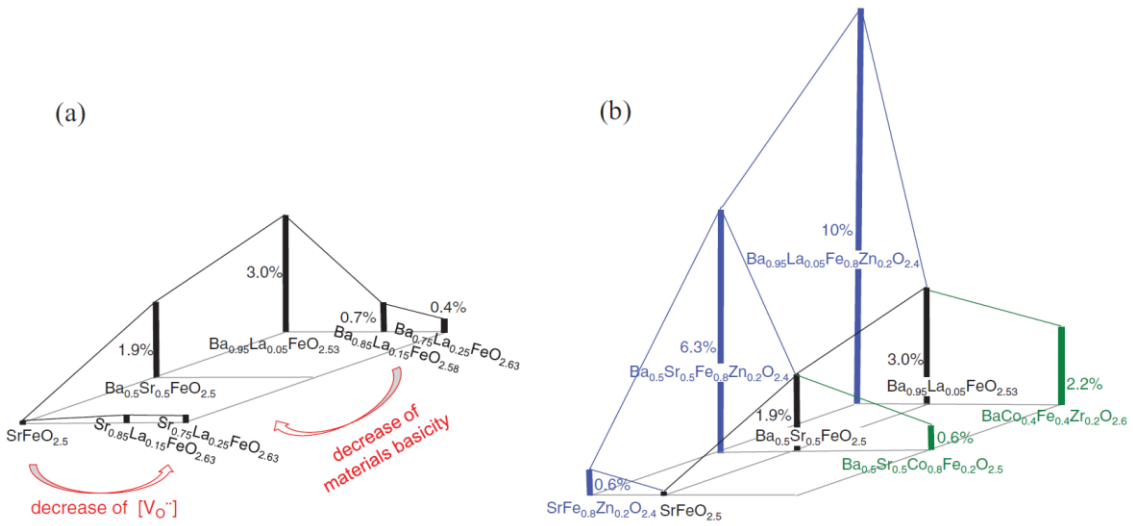

Figure 12. Proton concentration at 250 °C and ≈16 mbar H_2O. All materials are in the hydration regime. a) Variation of La and Sr content on the perovskite's A-site. b) Effect of Zn and Co substitution on the B-site. All panels reproduced with permission.[140] Copyright 2018, WILEY-VCH Verlag GmbH & Co. KGaA, Weinheim.

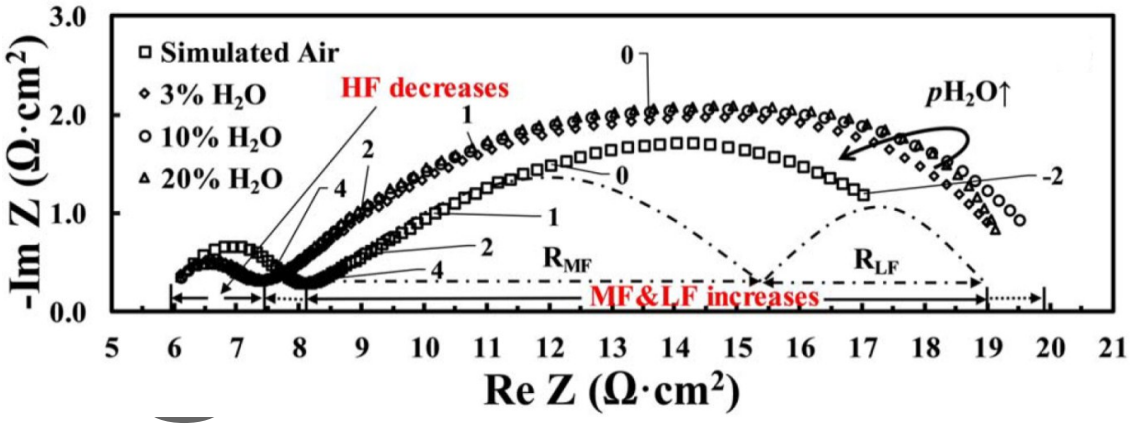

Figure 13. Impedance spectra for a BSCF/BCZYYb/BSCF symmetrical cell in dry simulated air (20%O_2/80%N_2 with <5 ppm H_2O or CO_2) versus simulated air humidified with various concentrations of moisture at 450 °C. Reproduced with permission.[144] Copyright 2017, The Electrochemical Society.

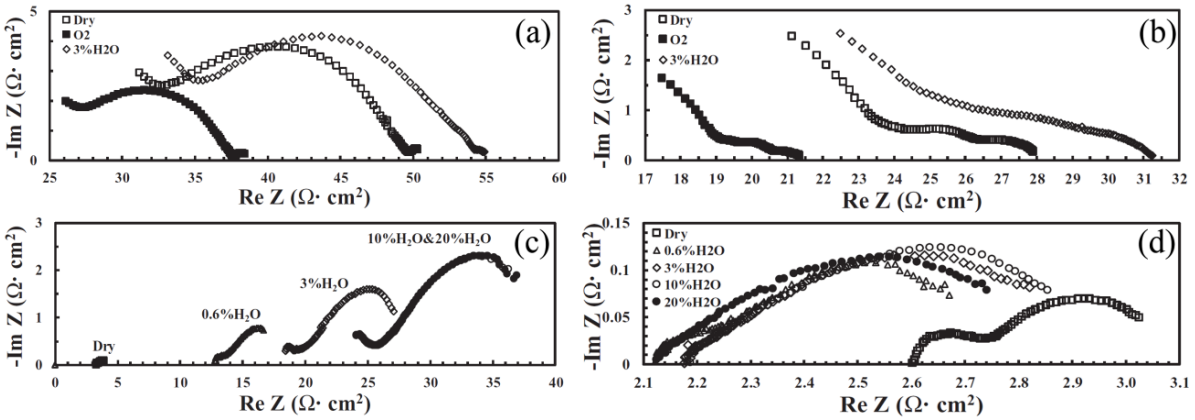

Figure 14. Impedance spectra for the symmetrical cells in dry simulated air (20%O_2/N_2 with <5ppm H_2O and CO_2) versus simulated air humidified with various concentrations of moisture at 450 °C in the case of the electrodes of Ag (a), LSFC (b), LSFC–BCZYYb (c) and BSCF (d). All panels reproduced with permission.[129] Copyright 2017, The Electrochemical Society.

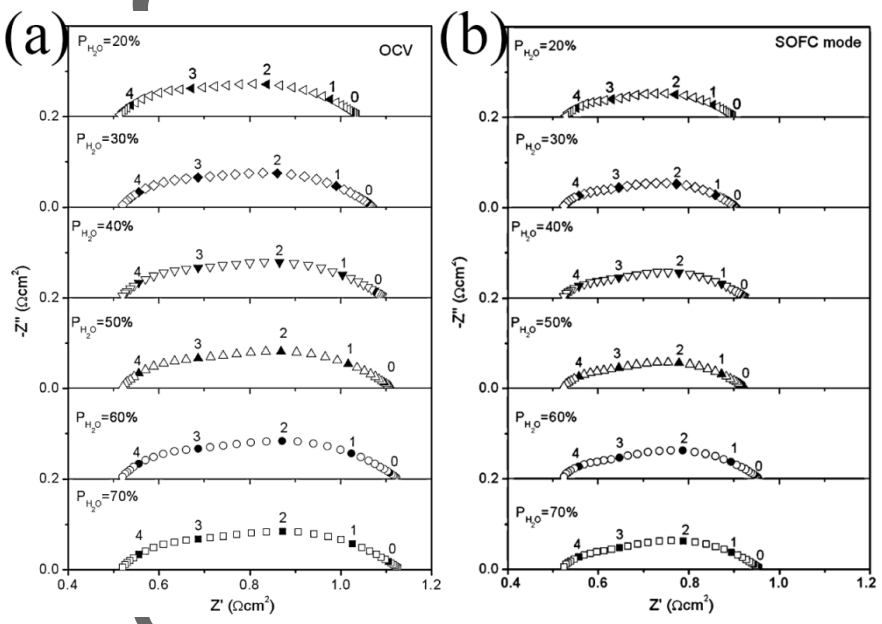

Figure 15. The impedance spectra of the Ni–BCZY0.3|BCZY0.3|SSC–BCZY0.3 cell at 700 °C in open circuit mode (U = OCV (a)) and SOFC mode (U = 0.7 V (b)) with various pH_2O levels in oxygen electrode. All panels reproduced with permission.[185] Copyright 2010, Elsevier.

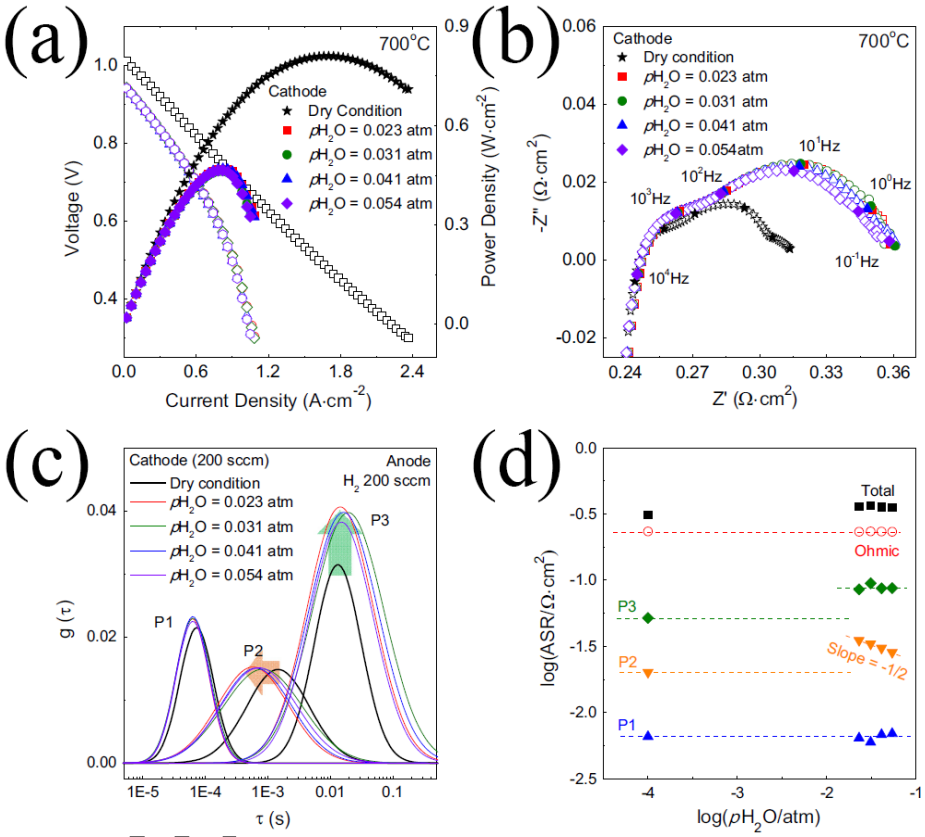

Figure 16. *I-V* and *I-P* curves for the Ni–BCZY0.4|BCZY0.4|BSCF fuel cell (a), its corresponding EIS spectra (b), DRT analysis (c) and total and constituent resistances depending on pH_2O at the cathode side (d). All panels reproduced with permission.[188] Copyright 2016, Elsevier.

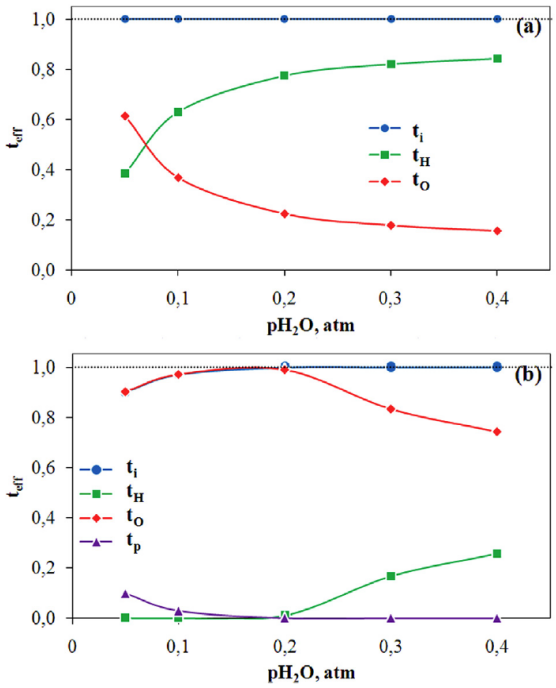

Figure 17. Effective transport numbers of protons, oxygen-ions and holes for BCGC material in SOFC mode at 600 °C (a) and 750 °C (b) and different water vapor pressure in $(1–x)H_2–xH_2O$ anode gas mixture. (a,b) Reproduced with permission.[189] Copyright 2016, Elsevier.

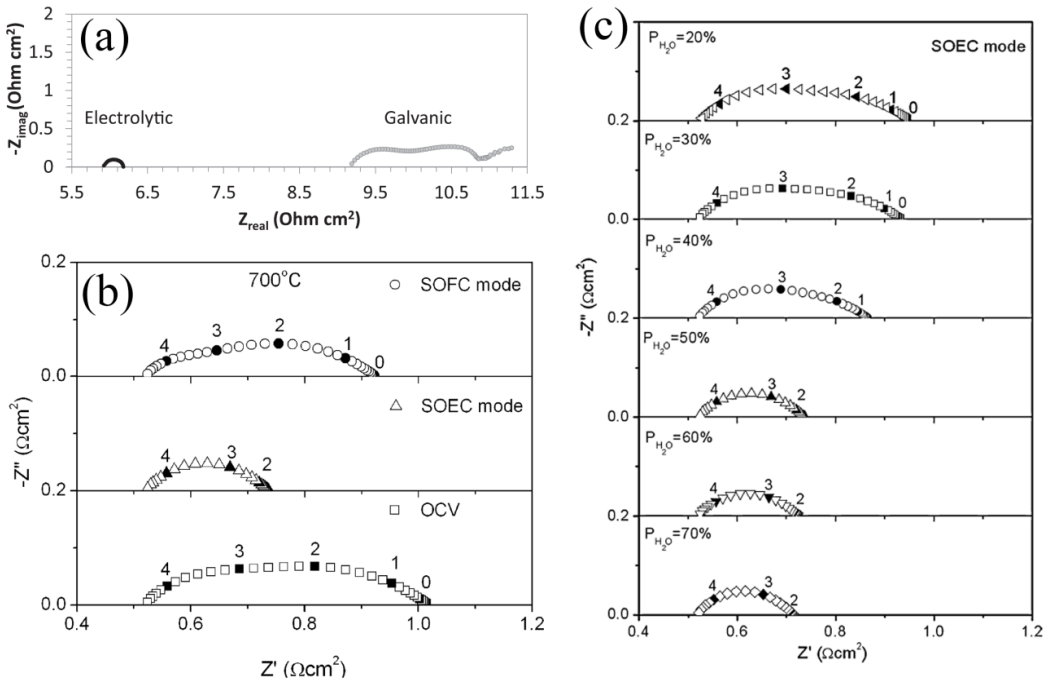

Figure 18. EIS spectra of the proton-conducing SOCs operating in fuel and electrolysis mode. (a) Ni–BCZY0.7|BCZY0.7 (25 µm)|LN (where BCZY0.7 = $BaCe_{0.2}Zr_{0.7}Y_{0.1}O_{3-\delta}$, LN = $La_2NiO_{4+\delta}$); Reproduced with permission.[193] Copyright 2015, Elsevier. (b) Ni–BCZY0.3|BCZY0.3 (20 µm)|SSC–BCZY0.3. (c) The impedance data for the same cell obtained at 700 °C in the electrolysis mode (1.3 V) with various pH_2O levels in oxygen electrode. All panels reproduced with permission.[185] Copyright 2010, Elsevier.

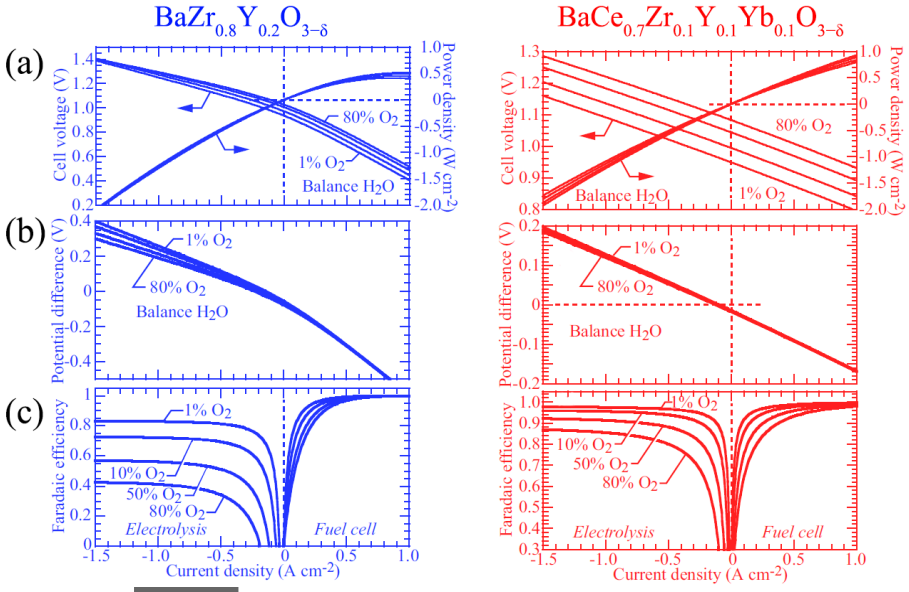

Figure 19. Predicted cell potentials, power density (a), electrolyte potential difference (b), and faradaic efficiency (c) of SOCs based on two well-known proton-conducting electrolytes as functions of current density at 600 °C and O_2+H_2O gas mixtures with different oxygen concentrations. The gas-phase composition on the fuel side is fixed as 97.0% H_2 and 3.0% H_2O. Four gas-phase compositions on the air side are 1.0%, 10.0%, 50.0%, and 80.0% O_2 balanced with H_2O. Reproduced with permission.[195,196] Copyright 2018, The Electrochemical Society.

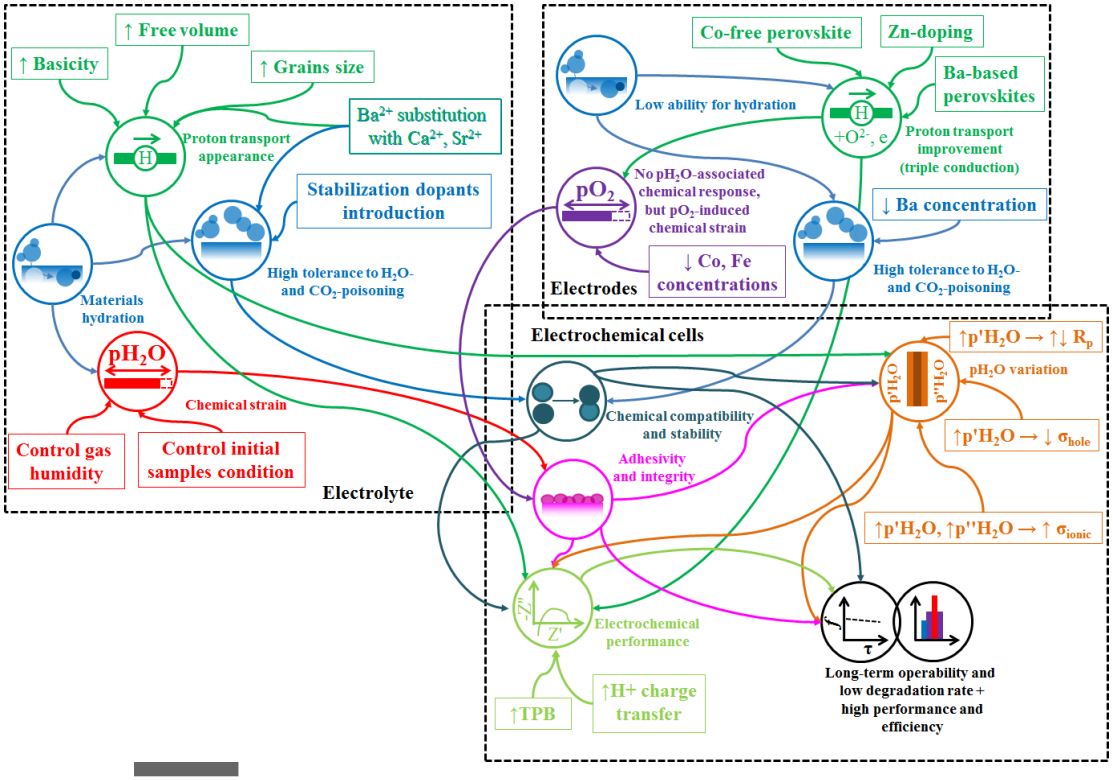

Figure 20. Influence of pH_2O on functionality of the individual materials and electrochemical cells based on them.

Table 1. The thermodynamic parameters of materials hydration.

No.	Material	ΔH [kJ mol^{-1}]	ΔS [J K^{-1} mol^{-1}]	Ref.
1	$BaCe_{0.9}Y_{0.1}O_{3-\delta}$	–138	–142	24
2	$BaCe_{0.9}Y_{0.1}O_{3-\delta}$	–122	–119	25
3	$BaCe_{0.9}Y_{0.1}O_{3-\delta}$	–123	–113	26
4	$BaCe_{0.9}Yb_{0.1}O_{3-\delta}$	–127	–126	25
5	$BaCe_{0.6}Zr_{0.3}Y_{0.1}O_{3-\delta}$	–106	–104	26
6	$BaCe_{0.4}Zr_{0.5}Y_{0.1}O_{3-\delta}$	–62.6	–70.1	27
7	$BaCe_{0.2}Zr_{0.7}Y_{0.1}O_{3-\delta}$	–93	–96	26
8	$BaZr_{0.9}Y_{0.1}O_{3-\delta}$	–79.5	–88.9	28
9	$BaZr_{0.9}Y_{0.1}O_{3-\delta}$	–83.3	–91.2	26
10	$SrCe_{0.95}Yb_{0.05}O_{3-\delta}$	–157	–128	29
11	$Ba_3Ca_{1.17}Nb_{1.83}O_{9-\delta}$	–65.2	–103.7	28
12	$Ba_3Ca_{1.18}Nb_{1.82}O_{9-\delta}$	–78.5	–111	30
13	$La_{0.9}Sr_{0.1}ScO_{3-\delta}$	–97	–112	31
14	$La_{0.9}Sr_{0.1}YbO_{3-\delta}$	–141	–111	32
15	$La_{0.9}Sr_{0.1}YO_{3-\delta}$	–90	–70	33
16	$La_{1.9}Ca_{0.1}Zr_2O_{7-\delta}$	–128	–150	34

Table 2. The crystal structure of $BaCe_{0.8-x}Zr_xY_{0.2}O_{3-\delta}$ perovskite materials at room temperatures: M – monoclinic, O – orthorhombic, R – rhombohedral, C – cubic.

x [concentration of zirconium]									Ref.
0	0.1	0.2	0.3	0.4	0.5	0.6	0.7	0.8	
M	n/a	n/a	R	n/a	R	n/a	n/a	C	38
M	O	O	O	O	O	C	C	C	39
O	n/a	C	C	C	C	C	C	C	40
R	R	R	R	C	C	C	C	C	41
C	C	C	C	C	C	C	C	C	42
O	O	n/a	n/a	C	C	C	C	C	43
O	O	O	R	C	C	C	C	C	44

Table 3. Some mechanical properties of proton-conducting perovskite materials: σ is the bending strength, H is the Vickers hardness, K_c is the fracture toughness, E is the Young's modulus, α is thermal expansion coefficient, marker * corresponds to the hydrated oxides.

Materials	σ [MPa]	H_v [GPa]	K_c [MPa $m^{1/2}$]	E [GPa]	α [$10^{-6}\times K^{-1}$]	Ref.
$SrCe_{0.95}Yb_{0.05}O_{3-\delta}$	150±20	5.5	2.1	n/a	11.5	89
$SrZr_{0.95}Yb_{0.05}O_{3-\delta}$	50±15	4.6	1.5	n/a	10.4	89
$BaCeO_3$	n/a	2.34	n/a	154	11.2	90
$Ba_3Ca_{1.18}Nb_{1.82}O_{9-\delta}$	110±10	5.0	1.0	n/a	12.3	89
$BaCe_{0.6}Zr_{0.2}Y_{0.2}O_{3-\delta}$	n/a	9.3	0.4	180	n/a	91
$BaZrO_3$	n/a	4.95	n/a	243	7.1	90
$BaZrO_3$	n/a	8.7	1.8	n/a	n/a	56
$BaZr_{0.9}Y_{0.1}O_{3-\delta}$	n/a	9.0	1.9	n/a	n/a	56
$BaZr_{0.9}Y_{0.1}O_{3-\delta}$*	n/a	10.0	2.4	n/a	n/a	56
$BaZr_{0.8}Y_{0.2}O_{3-\delta}$	n/a	8.0	1.8	n/a	n/a	56
$BaZr_{0.8}Y_{0.2}O_{3-\delta}$*	n/a	8.3	2.4	n/a	n/a	56
$BaCe_{0.2}Zr_{0.7}Y_{0.1}O_{-\delta}$	n/a	8.6	1.7	n/a	n/a	56
$BaCe_{0.2}Zr_{0.7}Y_{0.1}O_{-\delta}$*	n/a	8.4	2.8	n/a	n/a	56

Table 4. The average TECs for $BaCeO_3$-, $BaZrO_3$- and $BaCeO_3$–$BaZrO_3$-based proton conductors in ambient or dry and wet* air.

Composition	Temperature interval [°C]	average TECs×10^6 [K^{-1}]	Ref.
$BaCe_{0.5}Zr_{0.3}Yb_{0.2}O_{3-\delta}$	100–560	11.7	93
	560–900	7.6	
$BaCe_{0.5}Zr_{0.3}Y_{0.2}O_{3-\delta}$	100–575	10.8	93
	575–900	8.5	
$BaCe_{0.8}Y_{0.2}O_{3-\delta}$	100–620	11.6	44
	620–900	8.3	
	100–900	9.9	49
	100–900	11.1*	
$BaCe_{0.8}Gd_{0.2}O_{3-\delta}$	20–1000	9.8	94
$BaCe_{0.8}Sm_{0.2}O_{3-\delta}$	600–900	9.3	95
	20–800	10.3	96
	20–900	10.2	97
$BaCe_{0.7}Zr_{0.1}Y_{0.2}O_{3-\delta}$	20–630	11.3	98
	630–900	8.4	
	20–1000	11.2	99
	30–1000	13.5	100
$BaCe_{0.7}Zr_{0.1}Y_{0.1}Yb_{0.1}O_{3-\delta}$	50–650	12.1	101
	650–800	5.7	
	800–1000	8.5	
	10–500	14.2	102
	600–700	5.4	
	800–1100	11.6	
	20–1200	9.1	103
	20–1200	9.8*	

$BaCe_{0.4}Zr_{0.4}Y_{0.2}O_{3-\delta}$	500–900	8.5	44
	500–900	9.6*	
$BaZr_{0.8}Y_{0.2}O_{3-\delta}$	100–900	8.2	44
	100–900	8.0	49
	100–900	9.7*	
$BaZr_{0.9}Y_{0.1}O_{3-\delta}$	100–900	7.4	49
	100–900	8.8*	

Table 5. The main elementary steps for oxygen electrodes of SOFCs based on oxygen-ionic and protonic electrolytes. Reproduced with permission.[128] Copyright 2015, Elsevier. Abbreviations: g – gas, ads – adsorbed, el – electrode, e – electrolytes, int – interface, tpb – triple phase boundary, surf – surface.

Type of fuel cell	SOFC(O^{2-})		SOFC(H^+)
Model	I	II	III
Type of electrode	MIEC (O^{2-}/electron)	MIEC (O^{2-}/electron)	MIEC (H^+/electron)
Reaction step 1	$O_{2(g)} \rightleftarrows$	$O_{2(g)} \rightleftarrows$	$O_{2(g)} \rightleftarrows$
Reaction step 2	$O_{2ads} + 2e^{/} \rightleftarrows$	$O_{2ads} + 2e^{/} \rightleftarrows$	$O_{2ads} + 2e^{/} \rightleftarrows$
Reaction step 3	$O^{2-}_{2ads} \rightleftarrows$	$O^{2-}_{2ads} \rightleftarrows$	$O^{2-}_{2ads} \rightleftarrows$
Reaction step 4	$O^{-}_{ads} + e^{/} \rightleftarrows$	$O^{-}_{ads} + e^{/} \rightleftarrows$	$O^{-}_{ads} + e^{/} \rightleftarrows$
Reaction step 5	$O^{2-}_{ads} + v_{(el)} \rightleftarrows$	$O^{2-}_{ads} + v_{(el)} \rightleftarrows$	$H^{+}_{(e)} \rightleftarrows$
Reaction step 6	$O^{2-}_{(el)} \rightleftarrows$	$O^{2-}_{(el)} \rightleftarrows$	$H^{+}_{(int)} \rightleftarrows$
Reaction step 7	$O^{2-}_{(int)} \rightleftarrows$	$H^{+}_{(e)} \rightleftarrows$	$2H^{+}_{(el,surf)} + O^{2-}_{ads} \rightleftarrows$
Reaction step 8		$O^{2-}_{(tpb)} + 2H^{+}_{(tpb)} \rightleftarrows$	$H_2O_{ads} \rightleftarrows$
Reaction step 9		$H_2O_{(tpb)} \rightleftarrows$	

Table 6. The R_p values of the various oxygen electrodes under air humidification in a symmetrical cell configuration *(electrode|electrolyte|electrode)*. Abbreviations: BCZYYb = $BaCe_{0.7}Zr_{0.1}Y_{0.1}Yb_{0.1}O_{3-\delta}$, BCY = $BaCe_{0.9}Y_{0.1}O_{3-\delta}$, BCS = $BaCe_{0.8}Sm_{0.2}O_{3-\delta}$, BZY = $BaZr_{0.8}Y_{0.2}O_{3-\delta}$, BCZY = $BaCe_{0.7}Zr_{0.1}Y_{0.2}O_{3-\delta}$, BZCY = $BaZr_{0.7}Ce_{0.2}Y_{0.1}O_{3-\delta}$, BCGC = $BaCe_{0.89}Gd_{0.1}Cu_{0.01}O_{3-\delta}$, BSCF = $Ba_{0.5}Sr_{0.5}Co_{0.8}Fe_{0.2}O_{3-\delta}$, LSFC = $La_{0.6}Sr_{0.4}Fe_{0.8}Co_{0.2}O_{3-\delta}$, PBC = $PrBaCo_2O_{5+\delta}$, PBCF = $PrBaCo_{0.5}Fe_{1.5}O_{5+\delta}$, PN = $Pr_2NiO_{4+\delta}$, PCN = $Pr_{1.9}Ca_{0.1}NiO_{4+\delta}$, SSC = $Sm_{0.5}Sr_{0.5}CoO_{3-\delta}$, SSNC = $SrSc_{0.175}Nb_{0.025}Co_{0.8}O_{3-\delta}$, BSFC = $Ba_{0.5}Sr_{0.5}Fe_{0.8}Cu_{0.2}O_{3-\delta}$, BGLC = $BaGd_{0.8}La_{0.2}Co_2O_{6-\delta}$, YCBC = $Y_{0.8}Ca_{0.2}BaCo_4O_{7+\delta}$.

Electrolyte	Electrode	pH_2O change [atm]	R_p change [Ω cm^2]	Ref.
BZCY	BGLC	0.002 → 0.014, 650 °C, pO_2 = 1.5×10^{-4}	~13 → 8.3	128
BCY	LSCF	0.03 → 0.30 in air at 600 °C	12.5 → 17.0	136
BCY	BSCF	0.03 → 0.30 in air at 600 °C	3.75 → 2.25	136
BCY	PBC	0.03 → 0.30 in air at 600 °C	0.57 → 0.38	136
BCY	PN	0.03 → 0.30 in air at 600 °C	0.9 → 0.3	136
BCS	SSC–BCS	0.03 → 0.30 in air at 500 °C	10 → 8.5	137
BZY	LSFC	0.03 → 0.15 in N_2 at 600 °C	0.65 → 1.21	138
BZY	LSFC–BCY	0.03 → 0.15 in N_2 at 600 °C	0.49 → 0.97	138
BCY	PBC	0.03 → 0.30 in air at 600 °C	~0.6 → 0.4	139
BCY	PBCF	0.03 → 0.30 in air at 600 °C	7.2 → 8.3	139
BCZYYb	BSCF	10^{-6} → 0.03 in air	0.49 → 0.72 (650 °C) 2.99 → 3.83 (550 °C) 14.07 → 16.2 (450 °C)	144
BCZY	SSNC	0.03 → 0.30 in air at 600 °C	2.10 → 0.31	156
BCZY	BSFC–BCZY	0.03 → 0.30 in air at 600 °C	8.5 → 8.1	157
BCGC	YCBC	$4\cdot10^{-4}$ → 0.10 in air at 700 °C	0.49 → 1.05	158
BCGC	PCN–BCGC	$4\cdot10^{-4}$ → 0.10 in air at 700 °C	0.28 → 0.39	158

Table 7. The main characteristics of the Ni–BCZY0.3|BCZY0.3|SSC–BCZY0.3 fuel cell at 700 °C with various pH_2O levels in oxygen electrode.[185]

pH_2O [atm]	OCV [V]	E_{theor} [V]	OCV/E_{theor}	PPD [mW cm^{-2}]	Open-circuit mode, U = OCV		Fuel cell mode, U = 0.7 V	
					R_p [Ω cm^2]	R_O [Ω cm^2]	R_p [Ω cm^2]	R_O [Ω cm^2]
0.2	1.01	1.035	0.975	289	0.46	0.52	0.39	0.52
0.3	1.00	1.016	0.984	254	0.49	n/a	0.41	n/a
0.5	0.95	0.987	0.963	234	0.52	0.51	0.43	0.51
0.7	0.88	0.962	0.915	208	0.55	0.52	0.45	0.52

Table 8. Electrochemical data for the cells with a configuration of Ni-BCZD|BCZD|YBCZ, in wet H_2 and wet air atmospheres at 700 °C depending on humidity of gases: $p'H_2O = p''H_2O = 0.03$ atm (1) and $p'H_2O = p''H_2O = 0.10$ atm (2): E_O is the thermodynamic voltage value for ideal oxygen-conducting electrolyte, E_{sens} is the potential recorded by the oxygen sensor, E_{exp} is the measured OCV, R_e is the electronic resistance of the electrolyte, R_o is the total ohmic resistance of the electrolyte, $\sigma_{film,\ total}$ is the total film conductivity of the electrolyte, R_p is the polarization resistance of the electrode, R_{total} is the total cell's resistance and $\overline{t}_{i,corr}$ is the average transport numbers of ions. Reproduced with permission.[191] Copyright 2017, American Chemical Society.

Parameters	PPD [mW cm^2]	E_O [V]	E_{sesn} [V]	E_{exp} [V]	R_e [Ω cm^2]	R_o [Ω cm^2]	$\sigma_{film,\ total}$ [mS cm^{-1}]	R_p [Ω cm^2]	R_{total} [Ω cm^2]	$\overline{t}_{i,corr}$
Condition (1)	331	1.118	1.114	0.946	3.82	0.49	4.1	0.18	0.67	0.87
Condition (2)	313	1.063	1.060	1.001	5.27	0.42	4.8	0.36	0.79	0.92
Relative difference, %	–5.5	–4.9	–4.8	+5.8	+38.0	+14.3	+17.1	–100	–17.9	+5.7

Author Biographies and Photographs

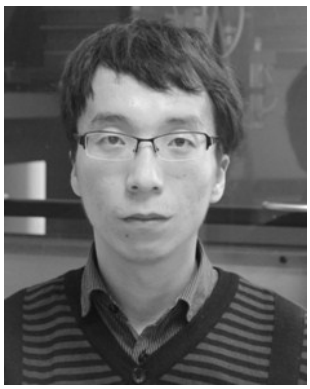

Wei Wang is a research fellow at Curtin University, Australia. He obtained his Ph.D. degree in Chemical Engineering at Nanjing Tech University, China, in 2013. His research interests include anode catalytic materials and coke formation mechanism for solid oxide fuel cells (SOFCs) operating on hydrocarbons, fuel selection and application for SOFCs, photocatalysts for the degradation of organic substances, photoanodes and photocathodes for dye-sensitized solar cells (DSSCs) and light absorbers for perovskite solar cells.

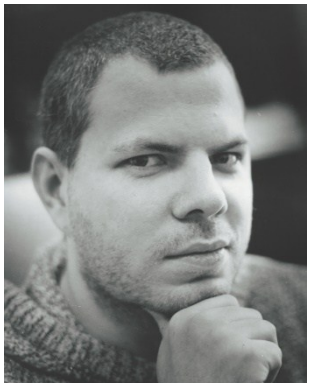

Dmitry Medvedev is a materials scientist, currently working as a senior researcher in the Laboratory of Electrochemical Devices based on Solid Oxide Proton Electrolytes (Institute of High Temperature Electrochemistry) and as a senior researcher in the Department of Environmental Economics (Ural Federal University). His research interests include designing, characterizing and applying the solid

oxide materials as membranes for various electrochemical devices, especially ones based on proton-conducting systems.

Zongping Shao is a professor of chemical engineering at Curtin University, Australia and Nanjing Tech University, China. He obtained his PhD from Dalian Institute of Chemical Physics, China in 2000. He worked as a visiting scholar at Institut de Researches Sur La Catalyse, CNRS, France and postdoc at California Institute of Technology, USA from 2000 till 2005. His current research interests include solid-oxide fuel cells, lithium-ion batteries, oxygen-permeable membranes and low-temperature energy-conversion devices.

Proton-conducting solid oxide cells (SOCs) have attracted much attention recently due to its high efficiency, low operating temperatures and zero environmental impact. This review provides an overview of the gas humidification impact on the operability and performance of SOCs in electrolysis and fuel cell modes. The material design strategies, degradation mechanism and perspectives of proton-conducting SOCs are also outlined.

Toc Keyword: Solid Oxide Electrochemical Cells

W. Wang, D. Medvedev*, Z. Shao*

Gas Humidification Impact on the Properties and Performance of Perovskite-Type Functional Materials in Proton-Conducting Solid Oxide Cells

ToC figure